J. Fluid Mech. (2009), *vol.* 631, *pp.* 65–102. © 2009 Cambridge University Press
doi:10.1017/S0022112009006740 Printed in the United Kingdom

Gravity currents impinging on bottom-mounted square cylinders: flow fields and associated forces

E. GONZALEZ-JUEZ[1], E. MEIBURG[1]† AND G. CONSTANTINESCU[2]

[1]Department of Mechanical Engineering, University of California at Santa Barbara, Santa Barbara, CA 93106-5070, USA

[2]Department of Civil and Environmental Engineering, University of Iowa, Iowa City, IA 52242, USA

(Received 25 January 2008 and in revised form 9 February 2009)

The unsteady drag and lift generated by the interaction of a gravity current with a bottom-mounted square cylinder are investigated by means of high-resolution Navier–Stokes simulations. Two-dimensional simulations for Reynolds numbers (Re) $O(1000)$ and three-dimensional simulations for $Re = O(10\,000)$ demonstrate that the drag coefficient increases exponentially towards a maximum as the current meets the cylinder, then undergoes strong fluctuations and eventually approaches a quasi-steady value. The simulation results show that the maximum drag coefficient can reach a value of 3, with the quasi-steady value being $O(1)$, which should aid in selecting a design drag coefficient for submarine structures under the potential impact of gravity currents. The transient drag and lift fluctuations after impact are associated with the Kelvin–Helmholtz vortices in the mixing layer between the gravity current and the ambient fluid. As these vortices pass over the cylinder, they cause the convection of separated flow regions along the bottom wall towards the cylinder. In two-dimensional simulations at $Re = O(10\,000)$, these flow structures are seen to be unrealistically coherent and to persist throughout the interaction, thus resulting in a noticeable overprediction of the drag and lift fluctuations. On the other hand, the impact of the current on the cylinder is seen to be very well captured by two-dimensional simulations at all Re values. Three-dimensional simulations lead to excellent agreement with available experimental data throughout the flow/structure interaction. They show that the spanwise variation of the drag is determined by the gravity current's lobe-and-cleft structure at impact and by an unsteady cellular flow structure similar to that found in constant-density flows at later times. A comparison between gravity-current flows and corresponding constant-density flows shows the hydrostatic drag component to be important for gravity currents.

1. Introduction

Gravity currents form in many natural environments and engineering applications when a heavier fluid propagates into a lighter one in a predominantly horizontal direction (Simpson 1997). Such currents are called compositional when driven by concentration variations of liquids, solutes or gases, or they are called particle-laden when the density differences result from differential particle loading. Of particular interest in the present context are particle-laden currents that form as a result of

† Email address for correspondence: meiburg@engineering.ucsb.edu

underwater landslides. The subsequent flow of sediment-laden fluid is referred to as a turbidity current. While such currents occur infrequently and unpredictably and often in remote environments, they can be extremely large and hence destructive of submarine equipment. Their interaction with submarine engineering structures, such as oil and gas pipelines, wellheads and submarine cables, poses a challenge to design engineers who require estimates of the dynamic loads and the associated time scales. Towards this end, high-resolution numerical simulations can be of great value, as they can provide access to quantitative information that may be difficult to obtain experimentally. Specifically, simulations have the capability to identify and track time-dependent flow features, along with simultaneous force fluctuations on the submerged structures. The knowledge gained from an investigation of turbidity current-structure interaction will be applicable to other areas as well, such as devices intended to protect from powder-snow avalanches (Hopfinger 1983).

A distinguishing ingredient in the interaction between turbidity currents and submarine structures lies in the unsteady nature of the governing dynamical processes. The largest forces and/or moments are expected to act on the structure when it is first encountered by the current head. Hence, a quantitative analysis has to focus on the processes during the impact of a front on the obstacle. In contrast, most of the past work on flow-structure interaction has addressed the problem of constant-density uniform flow past cylinders (cf. the review by Williamson 1996), along with the related area of vortex-induced vibrations (Williamson & Govardhan 2004). While a few investigations have addressed the issue of submerged objects impulsively started from rest (e.g. Koumoutsakos & Leonard 1995), the flow fields generated under such conditions are still fundamentally different from those to be considered here.

A second line of research on flow-structure interactions, relevant to the type of flows to be considered here, has focused on solid objects moving through stratified environments (e.g. Chomaz, Bonneton & Hopfinger 1993). Here, the emphasis has been both on the generation of internal waves by moving objects and on the near-field turbulence and far-field wake structure. Investigations have been conducted both for towed obstacles and for self-propelled ones in which there is no net force acting on the body. A detailed description of the relevant fluid dynamical mechanisms is provided by Spedding, Browand & Fincham (1996). Of some relevance to the type of flows considered here are also studies of weakly stratified flows past bottom-mounted obstacles, in which the force component due to the generation of waves is not important (e.g. Chernyshenko & Castro 1996; Castro 2002).

Very few investigations to date have explored the interaction between a gravity current and an obstacle at a fundamental level. Among them are the investigations by Greenspan & Young (1978), Rottman *et al.* (1985) and Lane-Serff, Beal & Hadfield (1995), whose shallow-water analyses are motivated by the need to design protective barriers against the accidental release of hazardous dense gases. This simplified approach enables them to predict a relation between the obstacle height and the fraction of the incoming gravity current that overruns the containment barrier. However, a detailed description of the current structure during the initial impact on the submerged cylinder cannot be obtained from shallow-water theory, so that it is questionable as to whether time-dependent force loads can be predicted on this basis. This is one of the issues to be addressed here.

Recent experimental investigations by Ermanyuk & Gavrilov (2005*a*, *b*) measure time-varying drag and lift coefficients of gravity-current flows over circular and square cylinders, separated by a gap from the bottom wall. Preliminary two-dimensional simulations by the present authors show good agreement with these experimental

data for circular cylinders, during the early stages of the interaction (Gonzalez-Juez, Constantinescu & Meiburg 2007). The experimental work identifies three distinct stages during the current-structure interaction, viz. an impact stage, a transient oscillatory stage and a quasi-steady stage. As the current approaches the cylinder, the drag is seen to increase monotonically with time in an exponential fashion, until it saturates and reaches a first maximum. The time at which it occurs is taken as the end of the impact and the beginning of the transient stage. A few successively smaller fluctuations define the subsequent transient stage, before the drag eventually settles down to a slowly decaying value during the quasi-steady stage. The drag force during the initial impact stage is found to be notably higher than during the later quasi-steady stage. The effects of the Reynolds and Schmidt numbers on the force coefficients are found to be almost negligible for the ranges investigated. The experimental methods do not provide a detailed description of the flow field, so that the forces cannot be correlated to specific flow structures. Establishing the link between the time-dependent flow field and the instantaneous force coefficients represents a main goal of the present investigation. The present investigation will primarily focus on configurations without a gap between the cylinder and the wall. However, results from one three-dimensional simulation with a gap will be presented and compared to experimental measurements.

It is known from both experiments (Bonnecaze & Lister 1999; Bonnecaze, Huppert & Lister 2006) and simulations (Härtel, Meiburg & Necker 2000; Necker *et al.* 2002, 2005; Ooi, Constantinescu & Weber 2005) that during the constant-velocity phase compositional and particle-driven currents share many features. In order to eliminate the complication of sedimentation and erosion, we will hence focus on a compositional gravity current in order to gain some insight into the processes governing the flow-structure interaction. Specifically, we will employ the generic case of a constant-velocity Boussinesq current in the lock-exchange configuration, which will be defined below (Huppert & Simpson 1980; Rottman & Simpson 1983).

Our primary objective is to identify, through a parametric study, the relation between flow structures and forces acting on the cylinder, along with the key dimensionless parameters and the proper scales, during all three of the above stages. In addition, we aim to identify the conditions under which two-dimensional simulations are adequate and when three-dimensional effects become important. Towards this end, we consider moderate-Reynolds-number currents typical of laboratory experiments ($Re \sim 10^3$–10^4), rather than the very high-Reynolds-number currents that one might encounter in nature ($Re \sim 10^7$–10^9). In this way, we will be able to compare our computational results with existing experimental measurements. Results from both two- and three-dimensional simulations will show that important physical mechanisms depend only weakly on the Reynolds number.

The manuscript is organized as follows: Section 2 defines the geometrical set-up of the problem, along with the set of governing equations. Subsequently, § 3 presents results from two-dimensional simulations. The force coefficients and associated flow structures will be described as functions of the size of the cylinder in relation to the current height, as well as of the channel depth. Furthermore, the influence of the Reynolds number, the bottom wall boundary condition and the Schmidt number will be discussed. Section 4 discusses results from three-dimensional simulations. These results will be analysed to determine the range of validity of two-dimensional simulations, to discuss the effect of the Reynolds number and to identify the type of flow structure that produces spanwise drag variations. The forces during the impact stage will be analysed in § 5.1, and a comparison with constant-density flows

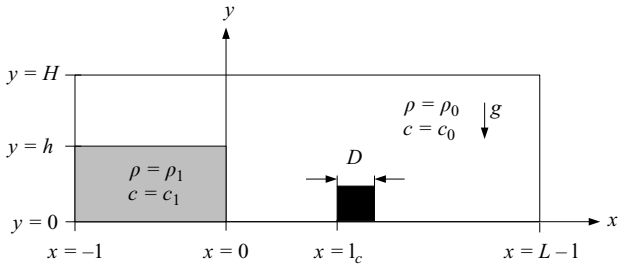

FIGURE 1. Schematic of the flow configuration. A channel of length L and height H contains a lock of length l and height h. When the gate at $x = 0$ is opened, a current of the denser fluid forms and propagates towards a square cylinder of side length D, which is situated a distance l_c away from the gate.

will be discussed in § 6. Finally, § 7 will briefly summarize the main findings and conclusions.

2. Problem description and computational approach

In order to address the objectives above, we conduct two- and three-dimensional numerical simulations of lock-exchange gravity currents interacting with bottom-mounted square cylinders. A square rather than a circular cylinder is chosen due to its relative simplicity from both physical and computational points of view. It is known from the study of constant-density flows past obstacles that the separation points on circular cylinders vary their location with time (Roshko 1993), whereas they remain fixed for square cylinders. Because of this fixed separation-point location, the flow around a square cylinder is expected to reach a regime of Reynolds number independence at lower values of the Reynolds number, as argued in Ermanyuk & Gavrilov (2005*a*), for example. The currents we consider are compositional in nature, with the density difference caused by differential concentration fields. Figure 1 shows a sketch of the channel of length L and height H, filled with ambient fluid of density ρ_0 and concentration c_0. Submerged in it is a lock of length l and height h, which contains the denser fluid of density ρ_1 and concentration c_1. When the vertical gate at $x = 0$ is opened, a current of the denser fluid forms and propagates towards the right along the floor of the channel. After travelling a distance l_c, it encounters a bottom-mounted cylinder of square cross-section, with side length D.

2.1. *Governing equations*

The simulations are based on the Navier–Stokes equations in the Boussinesq approximation, and they follow the approach outlined by Härtel *et al.* (2000) and Ooi *et al.* (2005). In the usual way, we introduce the buoyancy velocity

$$u_b = \sqrt{g'h}, \tag{2.1}$$

where the reduced gravity g' is defined as

$$g' = g(\rho_1 - \rho_0)/\rho_0. \tag{2.2}$$

The relationship between density and concentration is assumed to be linear:

$$\rho = \rho_0 + \frac{\rho_1 - \rho_0}{c_1 - c_0}(c - c_0). \tag{2.3}$$

By introducing suitable characteristic quantities, we can define dimensionless variables as

$$t^* = \frac{t}{(h/u_b)}\ ,\ x_i^* = \frac{x_i}{h}\ ,\ u_i^* = \frac{u_i}{u_b}\ ,\ p^* = \frac{p}{\rho_0 u_b^2}\ ,\ c^* = \frac{c - c_0}{c_1 - c_0}\ . \tag{2.4}$$

As a basis for large-eddy simulations (LESs) with subgrid-scale contributions to the diffusion of momentum and concentration, we thus obtain the governing dimensionless equations for the conservation of mass, momentum and concentration in the form

$$\frac{\partial u_j^*}{\partial x_j^*} = 0, \tag{2.5}$$

$$\frac{\partial u_i^*}{\partial t^*} + \frac{\partial u_i^* u_j^*}{\partial x_j^*} = -\frac{\partial p^*}{\partial x_i^*} + \frac{\partial}{\partial x_j^*}\left(\left(\frac{1}{Re} + \nu_{SGS}^*\right)\left(\frac{\partial u_i^*}{\partial x_j^*} + \frac{\partial u_j^*}{\partial x_i^*}\right)\right) + c^*\, e_i^g, \tag{2.6}$$

$$\frac{\partial c^*}{\partial t^*} + \frac{\partial c^* u_j^*}{\partial x_j^*} = \frac{\partial}{\partial x_j^*}\left(\left(\frac{1}{Re\ Sc} + \kappa_{SGS}^*\right)\frac{\partial c^*}{\partial x_j^*}\right). \tag{2.7}$$

Here u_i^* denotes the velocity vector, p^* the total pressure and c^* the concentration, and e_i^g indicates the unit vector pointing in the direction of gravity. The spatial coordinates are denoted either by (x, y, z) or by (x_1, x_2, x_3). As governing dimensionless parameters in (2.5)–(2.7) we identify the Reynolds and Schmidt numbers, respectively,

$$Re = \frac{u_b h}{\nu}\ ,\ Sc = \frac{\nu}{\kappa}, \tag{2.8}$$

where ν represents the kinematic viscosity and κ the molecular diffusivity. Note that the product of these two parameters yields the Péclet number, $Pe = Re\,Sc$. In addition, there are various geometrical parameters, the most important ones being H/h and D/h.

We remark that in the following discussion, it will generally be advantageous to render time dimensionless by means of the front velocity V, since this will frequently lead to a better collapse of data from different flow fields. Nevertheless, in deriving the above equations we employ u_b for non-dimensionalizing time, since this quantity is known *a priori*, whereas V can be determined only in the course of carrying out the numerical experiment. For the same reason, the lock height h is taken as the length scale rather than the gravity-current height. We note that the height of lock-exchange currents usually is close to $h/2$ (Shin, Dalziel & Linden 2004).

In § 3, we analyse results from several two-dimensional direct numerical simulations (DNSs). In these simulations all of the two-dimensional scales of motion are resolved by choosing a sufficiently fine grid and by setting the subgrid viscosity ν_{SGS}^* and diffusivity κ_{SGS}^* in (2.6) and (2.7) to zero. On the other hand, the three-dimensional simulations of § 4 employ an LES approach, so that a higher-Reynolds-number regime can be reached. With the LES approach, only the large energy-containing scales are resolved, while the effect of the small unresolved scales on the large scales is modelled by evaluating ν_{SGS}^* and κ_{SGS}^* in (2.6) and (2.7) with the dynamic Smagorinsky model (Germano *et al.* 1991; Lilly 1992). Additional details are provided in Pierce (2001) and Ooi, Constantinescu & Weber (2007). Comparisons of the two-dimensional DNS and three-dimensional LES results will allow us to assess the range of validity of two-dimensional simulations in § 4.

Unless otherwise stated, the bottom ($y = 0$) and left ($x = -l$) boundaries of the computational domain, and the surface of the cylinder, are treated as no-slip walls. The top boundary ($y = H$) is considered to be a slip wall. A convective boundary

Parameter	Reference case	Other values
L/h	24	
l/h	9	
l_c/h	3	
H/h	5	1, 1.25, 1.66, 2.5
Re (Re_D)	2000 (177)	4000, 10 000, 50 000
Sc	1	10
D/h	0.15	0.05, 0.1, 0.25, 0.4, 0.5, 0.6, 0.7, 0.8
Grid	2048×320	2048×256, 3000×400
$\mathrm{d}t/(h/u_b)$	0.002	

TABLE 1. Parameter values employed in the two-dimensional numerical simulations.

condition is employed along the right boundary ($x = L - l$) of the domain (Pierce 2001). In the three-dimensional simulations of § 4, the flow in the spanwise z-direction is assumed to be periodic. The flow field is initialized with the fluid at rest everywhere and the dimensionless concentration c^* being 1 within the lock and 0 outside it.

2.2. *Numerical methodology*

Equations (2.6)–(2.7) are discretized on a non-equidistant Cartesian mesh and solved with a finite-volume DNS/LES code (Pierce 2001; Pierce & Moin 2004) that has been extensively validated (Ooi *et al.* 2005, 2007). Preliminary two-dimensional results obtained with this code closely reproduce the experiments by Ermanyuk & Gavrilov (2005*b*) (cf. Gonzalez-Juez *et al.* 2007). Specifically, the maximum drag and maximum lift amplitude, which are defined later, are captured to within 10 % and 4 %, respectively. The simulation of irregular rectangular domains is accomplished by means of a grid blanking methodology. The velocity components are represented in a staggered fashion with respect to pressure and concentration, in both space and time. All differential operators are discretized using central differences, except for the convection term in the concentration conservation equation (2.7), which is discretized using the QUICK scheme. Time integration is accomplished via an iterative procedure similar to the Crank–Nicolson scheme. To ensure that the continuity equation (2.5) is satisfied, a Poisson equation for the pressure correction is solved at each time step by means of a multi-grid algorithm. The numerical method is second-order accurate in both space and time.

3. Results from two-dimensional simulations

Table 1 indicates the parameter ranges of the simulations. Unless stated otherwise, our discussion will refer to the reference case. The computational domain length is kept at $L/h = 24$ for all simulations. The constant lock length of $l/h = 9$ ensures that reflections from the left wall do not influence the interaction between the gravity-current front and the cylinder, during the time of the simulation. The distance between the gate and the cylinder is chosen as $l_c/h = 3$, so that the current is in the constant-front-speed phase when it encounters the cylinder. Both full-depth ($H/h = 1$) and partial-depth ($H/h > 1$) currents will be analysed. As will be seen, the case of $H/h = 5$ closely approximates the deep-ambient case of $H/h \to \infty$, in agreement with observations for gravity currents in the absence of submerged obstacles (Simpson

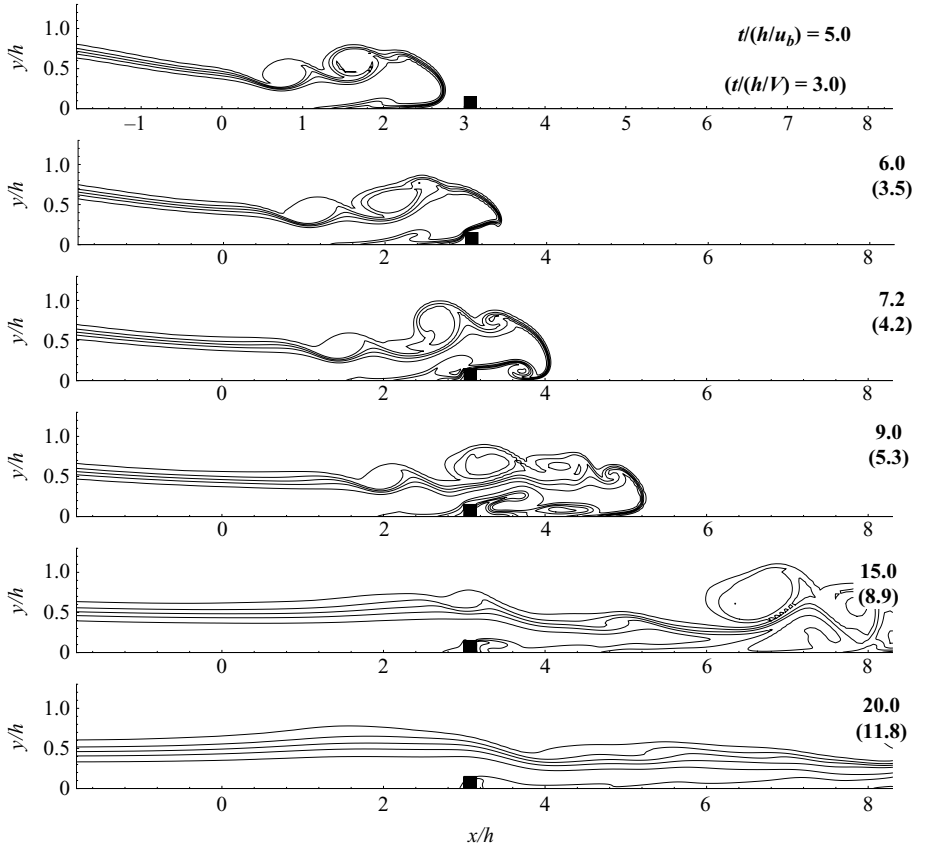

FIGURE 2. Interaction of a partial-depth ($H/h = 5$) gravity current with a cylinder of $D/h = 0.15$. The current is visualized by means of the $c^* = 0.1$, 0.3, 0.5, 0.7 and 0.9 concentration contours. As the current head is deflected upward by the cylinder, overshoots it and eventually reattaches again, recirculation regions form both upstream and downstream of the cylinder.

1997). Reynolds numbers up to 50 000 will be considered, which are typical of laboratory gravity currents. A relatively low value of $Re = 2000$ is selected as the reference case, since for Re values $O(10\,000)$ or larger two-dimensional simulations show a flow behaviour that is not consistent with experimental observations, as will be discussed in § 4. The Reynolds number $Re_D = VD/\nu$ based on the square side D and the gravity-current front velocity V has a value of 177 for the reference case; D/h is varied from 0.05 to 0.8. For comparison, typical gravity-current heights O(1–100 m) and cylinder length scales O(1 m) yield a range of $D/h = 0.005$–0.5. A grid of 2048×256 is employed for $H/h = 1$ and 1.25, while for other values of H/h the grid is 2048×320. For $Re \geqslant 4000$, the grid is further refined to 3000×400. This ensures a grid spacing of about $0.01D$ in the vicinity of the cylinder. The time step size is limited such as to keep the Courant–Friedrich–Lewy (CFL) number below a suitable value determined in test simulations. The parameter combinations of further simulations will be discussed later.

3.1. *Reference case: description of the flow field*

Figure 2 displays the interaction of the reference current with the bottom-mounted square cylinder. Initially, the current is seen to approach the cylinder from the left.

H/h	Re	Bottom boundary	V/u_b
5	2000	No slip	0.59
5	10 000	No slip	0.62
5	50 000	No slip	0.64
5	2000	Slip	0.68
1	2000	No slip	0.40

TABLE 2. Values of V/u_b during the constant-speed phase for different parameter combinations.

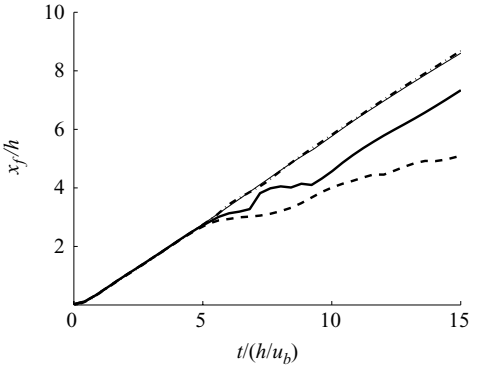

FIGURE 3. Gravity-current front position (x_f/h) versus time in partial-depth $H/h = 5$ currents for different values of D/h: 0.15 (dash-dotted line), 0.40 (thick solid line), 0.80 (dashed line) and without the cylinder (thin solid line).

We recognize the familiar structure of the head (see, among others, Simpson 1997; Härtel *et al.* 2000), as well as two large-scale, Kelvin–Helmholtz-type vortices at the interface that separates the current from the ambient fluid. As it encounters the cylinder, the current head is deflected upward. Inertia keeps it moving forward, and it eventually reattaches along the bottom wall several diameters downstream of the cylinder. Eventually, the flow reaches a quasi-steady state as the current head continues to propagate downstream of the cylinder.

The front position x_f/h, defined as the foremost location of the $c^* = 0.5$ contour, is shown as a function of time in figure 3 for the reference current, as well as various other values of D/h. The front speed can be inferred from the slope of the curve. After an initial transient, the front speed is seen to be constant and equal to the case without submerged cylinder, until the current reaches the vicinity of the cylinder around $t/(h/u_b) \approx 5$ ($t/(h/V) \approx 3$). Table 2 shows the value of the front speed V/u_b during the constant-speed phase for different parameter combinations. The current head then experiences a deceleration whose strength and duration depend on the size of the cylinder. Eventually, the current front speeds up again. Figure 3 shows that large obstacles reduce the post-interaction front velocity permanently.

Figure 4 provides detailed information on the temporal evolution of the concentration (left column) and vorticity (right column) fields for the reference case. Instantaneous streamlines in the laboratory reference frame are superimposed on the concentration field and yield additional insight into the flow structures. Following Ermanyuk & Gavrilov (2005*a*, *b*), we distinguish between the impact, transient and quasi-steady stages of the flow. Already before the current front reaches the cylinder,

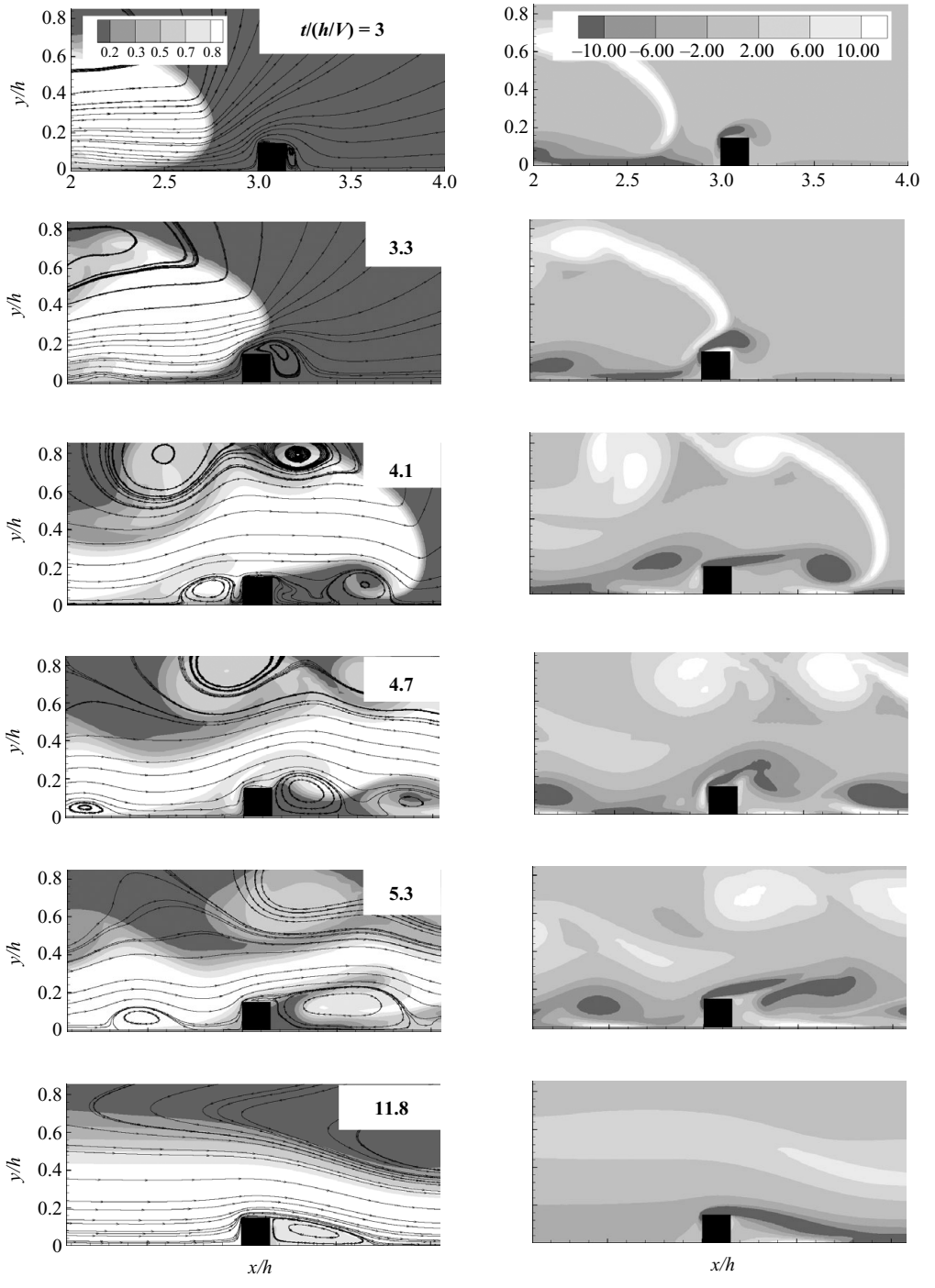

FIGURE 4. Temporal evolution of the concentration c^* (left) and vorticity $\omega/(V/h)$ (right) fields as the gravity current interacts with the square cylinder for the reference case. Instantaneous streamlines in the laboratory reference frame are superimposed on to the concentration fields.

it accelerates the fluid in its vicinity, thereby leading to the formation of a separated flow region above and behind the cylinder. The impingement of the current on the cylinder coincides with the transition from impact to transient stage. As the current impinges on the cylinder and is deflected upward, the separated flow region increases in size. Several diameters downstream of the cylinder, the current plunges downward and reattaches to the bottom wall. In this process, it traps some of the ambient fluid in the near wake of the cylinder. Eventually, the gravity current re-establishes itself downstream of the cylinder, and the quasi-steady stage begins. Note the difference in the depth of the dense fluid layer upstream and downstream of the cylinder during this quasi-steady stage, similar to the observation by Ermanyuk & Gavrilov (2005*a*).

Throughout the impact and transient stages, we observe the transient existence of separated flow regions both upstream and downstream of the cylinder. Such recirculation regions along the wall are known to exist even in the absence of a submerged cylinder (Härtel *et al.* 2000; Cantero *et al.* 2007; Ooi *et al.* 2007). When a cylinder is present, these regions approach the cylinder from far upstream. Similarly, the vortices that are shed on the downstream side of the cylinder are intermittently swept downstream. The effect of these recirculation regions on the forces affecting the cylinder will be analysed below.

3.2. *Drag, lift and torque as functions of time for the reference case and the effect of the cylinder size*

The force F_i exerted by the fluid on the cylinder can be evaluated as

$$F_i = \int_A -n_i(p - p_{ref}) + n_j\, \mu \left(\frac{\partial u_i}{\partial x_j} + \frac{\partial u_j}{\partial x_i} \right) \mathrm{d}A, \tag{3.1}$$

where A denotes the surface of the cylinder, n_j its outer normal and p_{ref} a reference pressure that depends on time only. We refer to the first term on the right-hand side of (3.1) as the pressure component and to the second term as the viscous component. In order to eliminate any effect of p_{ref} on the temporal fluctuations of F_i, we evaluate p_{ref} at $x = L - l$ and $y = H/2$, where the velocity is negligible throughout the simulation. The x- and y-component of F_i are referred to as drag F_D and lift F_L, respectively.

Figure 5(*a*) shows the variation of the drag with time for various cylinder sizes D/h. Note that F_D has been normalized by means of the cylinder size D rather than the lock height h, as this results in a better collapse of the data for different values of D/h. As the current approaches the cylinder, the drag is seen to increase monotonically with time in an exponential fashion, until it saturates and reaches a first maximum. The value of the drag at this first maximum is referred to as the maximum drag $F_{D,max}$. As stated earlier, the time at which it occurs is taken as the end of the impact and the beginning of the transient stage. Subsequently, the drag declines rapidly with time and reaches a pronounced minimum whose value decreases with the cylinder size and even drops below zero for $D/h = 0.05$. The dimensionless time of the drag minimum increases with the cylinder size. Successively smaller fluctuations follow during the transient stage, and the drag settles down to a slowly decaying value during the quasi-steady stage.

Figure 5(*a*) indicates that both maximum and quasi-steady drag increase with D/h. At first glance, this may appear at odds with available experimental measurements for rectangular cylinders, in which the maximum drag is seen to decrease with D/h, while its quasi-steady value remains approximately constant (figure 5*a* in Ermanyuk & Gavrilov 2005*a*). This apparent contradiction is due to differences in the way in which the dimensionless parameters are varied in the simulations and experiments. In the

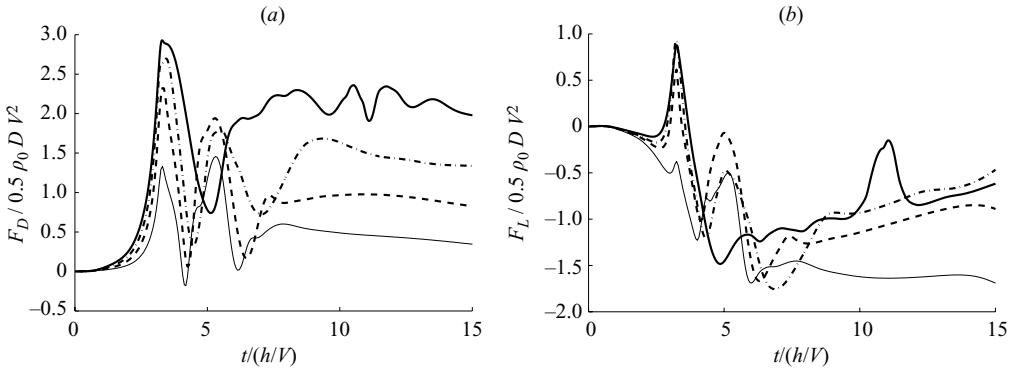

FIGURE 5. Effect of D/h on the time-dependent drag (a) and lift (b) in partial-depth $H/h = 5$ gravity currents: $D/h = 0.05$ (thin solid line), 0.15 (dashed line), 0.25 (dash-dotted line), 0.40 (thick solid line). All cases displayed pronounced drag (lift) fluctuations during the impact and transient stages, before settling down to a slowly decaying (increasing) value during the quasi-steady stage.

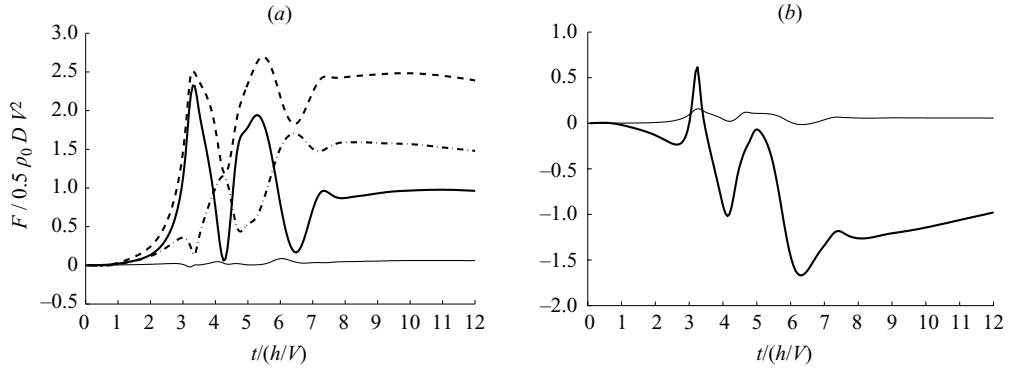

FIGURE 6. Temporal evolution of the drag (a) and the lift (b) for the reference case. Also shown in (a) are the pressure forces on the upstream F_w (dashed line) and downstream F_e (dash-dotted line) faces. The viscous drag and lift components (thin solid line) are much smaller than the pressure components.

simulations, D/h is varied, while H/h and Re are kept constant. In the experiments, on the other hand, D/h, H/h and Re are all varied simultaneously as a result of selecting the channel height as the length scale, rather than the lock height. Thus, the respective data do not describe comparable flow situations. A quantitative comparison to be discussed below, however, will show that if all three of the above parameters match the experimental values, two-dimensional simulations capture the impact stage quite accurately, while three-dimensional simulations are required to obtain appropriate force values for the quasi-steady stage, at high values of Re.

We will now relate the drag data to the flow-field structure. For the reference case, figure 6(a) shows both the overall drag force and its individual components due to the pressure forces on the upstream (F_w) and downstream (F_e) faces of the cylinder and the viscous drag force (F_v) acting on its top surface. The sign of the pressure forces is positive when directed from the fluid towards the solid wall. The overall drag is thus obtained as

$$F_D = F_w - F_e + F_v. \tag{3.2}$$

For all simulations, we found the viscous drag component to remain close to zero, so that the pressure forces on the upstream and downstream faces dictate the temporal evolution of the drag.

For the reference case, the time intervals for the impact, transient and quasi-steady stages are approximately $1 < t/(h/V) < 3.3$, $3.3 < t/(h/V) < 8.8$ and $t/(h/V) > 8.8$, respectively.

Closer inspection of figure 4 indicates that by $t/(h/V) = 3$ the flow has separated at the upstream top corner. Note also the small recirculation region that is forming downstream of the cylinder at this time. The transport of the negative vorticity generated at the upstream top corner into this recirculation region can be recognized at $t/(h/V) = 3$ in figure 4. Interestingly, this recirculation region on the downstream side is not primarily responsible for the drag maximum at $t/(h/V) \approx 3.3$. Rather, figure 6(a) shows that the first drag maximum is produced by the pressure increase on the upstream side, as the approaching gravity current decelerates and sets the fluid immediately upstream of the cylinder in motion.

Thereafter, as figure 6(a) shows, the drag decreases during the time interval $t/(h/V) \approx 3.3$–4.4 due to a combination of decreasing F_w and increasing F_e. The decrease in F_w results from the formation of a strong recirculation region upstream of the cylinder, which is seen in the $t/(h/V) = 4.1$ frame of figure 4. The $t/(h/V) = 3.3$ and $t/(h/V) = 4.1$ time frames of figure 4 also show how the recirculation region behind the cylinder is convected downstream and away from the obstacle, which contributes to the sudden increase in F_e and thus to the drag decrease.

During the time interval $t/(h/V) \approx 4.4$–5.3, a pronounced drag increase is observed. The vorticity field for $t/(h/V) = 4.7$ in figure 4 shows the clockwise vortex upstream of the cylinder being convected past the cylinder and into the recirculation region downstream of it. This process appears to be related to the passing of a Kelvin–Helmholtz billow. Hence the pressure force acting on the upstream face increases, while its downstream counterpart decreases. The drag thus reaches a second maximum at $t/(h/V) \approx 5.3$. Interestingly, the second drag maximum does not occur in the $H/h = 5$ and $D/h = 0.4$ cases, as can be seen from figure 5(a). Here the convection of negative vorticity past the cylinder does not occur, likely because of the blockage effect due to the relatively large cylinder.

Figure 5(a) shows that for the reference case the drag begins to decrease beyond $t/(h/V) \approx 11$. A similar decrease sets in at slightly different times for other parameter combinations. Our analysis generally focuses on the flow evolution before this effect becomes dominant.

Results for the variation of lift with time for different values of D/h are shown in figure 5(b). Note that, just as for the drag, we normalize the lift by means of the cylinder size D, rather than the lock height h, in order to obtain a better collapse of the data. As the current approaches the cylinder, the lift dips below zero, only to rise rapidly as the current reaches the cylinder. We observe that maximum lift and drag are reached nearly simultaneously at $t/(h/V) \approx 3.3$. Subsequently, the lift decreases dramatically to values below zero, indicating a downward force on the cylinder. For smaller cylinders, the maximum downward force is reached more quickly, similar to the drag, whereas the magnitude of the downward lift force depends only weakly on the cylinder size.

Figure 6(b) shows that, just as for the drag, the lift force is dominated by the pressure contribution, compared to which the viscous contribution is negligible. The lift is seen to reach an upward-directed maximum by $t/(h/V) \approx 3.3$. At this time, figure 4 shows a large recirculation region above and downstream of the

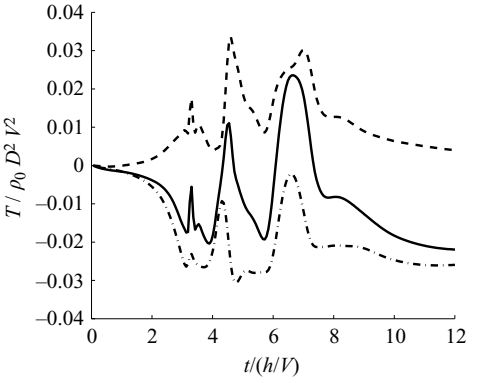

FIGURE 7. Temporal evolution of the torque (solid line) for the reference case. The contributions to the torque from the pressure (dashed line) and viscous (dash-dotted line) forces are seen to be of comparable magnitude.

cylinder. Thus, the initial increase of the lift is produced by the suction associated with the presence of this recirculation region above the cylinder. The $t/(h/V) = 3.3$ and $t/(h/V) = 4.1$ time frames of figure 4 show that this recirculation region is later convected downstream, resulting in a decrease of the lift (cf. figure 6*b*). By $t/(h/V) \approx 4.1$ the lift reaches a downward extremum. In addition, this decrease of the lift is also produced by an increase of the hydrostatic pressure on top of the cylinder, as the dense fluid engulfs the cylinder. The subsequent increase in the lift during the interval $t/(h/V) \approx 4.1$–5 is again related to the convection of an intense vorticity region past the top surface of the cylinder (cf. figure 4). As this patch of vorticity enters the downstream recirculation region, the lift decreases again during $t/(h/V) \approx 5$–6.2. Eventually, the lift reaches a negative quasi-steady state value, whose value can be estimated as follows: Initially, the hydrostatic pressure on top of the cylinder is $\rho_0 g(H - D)$. During the quasi-steady state stage, the height of the dense fluid layer engulfing the cylinder is approximately $h/2$ (cf. figure 4). This gives a hydrostatic pressure on top of the cylinder of $\rho_0 g(H - h/2) + \rho_1 g(h/2 - D)$. The quasi-steady state lift results from the difference of these hydrostatic pressures, and we obtain $F_{L,st}/0.5\rho_0 D u_b^2 = -1 + 2(D/h)$. This expression provides a rough estimate.

The above results indicate that by scaling the dimensionless drag and lift with D, they remain of the same order when varying D/h. We will further discuss the hydrostatic ($\rho_0 h u_b^2$ or equivalently $\rho_0 h g' h$) and dynamic ($\rho_0 D V^2$) components of the drag in §§ 5.2 and 6.

Figure 7 displays the temporal variation of the torque around the geometric centre of the cylinder. Also indicated are the individual contributions to the torque from pressure and viscous forces. Interestingly, even though figure 6 showed pressure forces to be an order of magnitude larger than viscous forces, their contributions to the torque are comparable. This reflects the larger lever of the viscous forces, which act tangentially on each surface. Close inspection of the pressure profile along each surface, on the other hand, shows a fairly uniform distribution, which implies a small torque. Based on the small value of the torque, it can be assumed with good accuracy that the force vector acts on the cylinder through its geometric centre. For practical applications, this simplifies the stress calculation on the foundation of the submerged structure. The fact that the torque, when scaled as $T/\rho_0 D^2 V^2$, is $O(10^{-2})$ suggests that

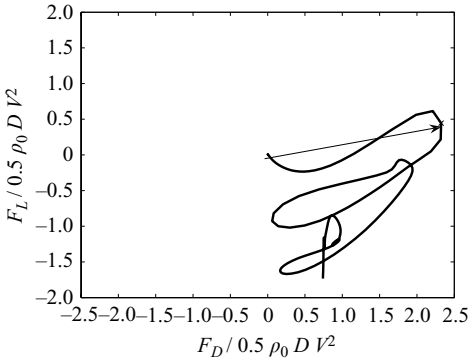

FIGURE 8. Hodograph of the tip of the force vector for the reference case. The force vector is directed downstream and downward most of the time.

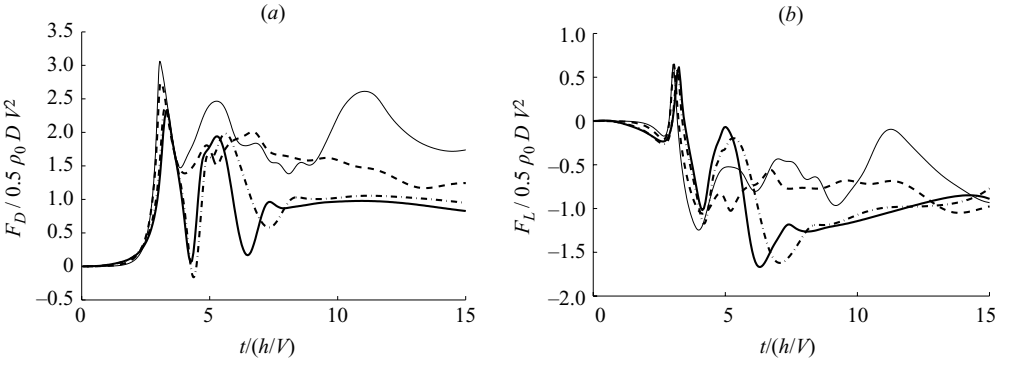

FIGURE 9. Effect of H/h on the total drag (a) and lift (b) variation with time: $H/h = 1$ (thin solid line), 1.25 (dashed line), 2.5 (dash-dotted line), 5 (thick solid line). The largest dimensionless drag is obtained for the full-depth case.

it may be more instructive to use a different scaling. We note that when including the dynamic viscosity μ in the scaling of the torque, we obtain that $T/\mu DV$ is $O(1)$.

A hodograph of the force vector is shown in figure 8 for the reference case. The maximum force vector is shown in this figure, where it can be seen to form an angle of 10.9° with the horizontal axis. Not surprisingly, the maximum force vector was observed to occur at the time of the maximum drag ($t/(h/V) = 3.3$). Interestingly, while the maximum force vector is directed downstream and upward, figure 8 shows that the force vector is directed downstream and downward most of the time. In practical applications, this information might be useful for design purposes of submarine structures under the potential impact of gravity currents.

3.3. *Effect of the channel depth*

Figure 9(a) shows the drag as function of time for $D/h = 0.15$ and different channel depths H/h. The data collapse most closely if the front velocity V, rather than the buoyancy velocity u_b, is employed to normalize F_D and time. This reflects the dependence of the front velocity on H/h (Benjamin 1968; Simpson 1997). The largest dimensionless drag is observed for the full-depth case, $H/h = 1$. Note that the curves for $H/h = 5$ and 2.5 track each other closely during the impact stage, which indicates that for a channel depth of 2.5 times the lock depth we already approach the deep ambient case.

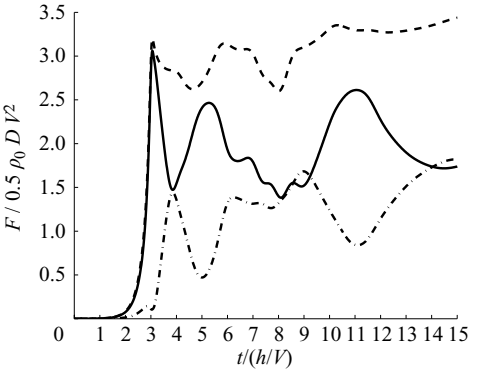

FIGURE 10. Temporal evolution of the drag for the full-depth $H/h=1$ case. Also shown are the pressure forces on the upstream F_w (dashed line) and downstream F_e (dash-dotted line) faces. In contrast to the partial-depth case, the upstream pressure force for the full-depth case fluctuates only mildly after reaching its first maximum.

Figure 9(a) shows that, after the first drag maximum, the drag fluctuates more strongly for the partial-depth $H/h=5$ case, as compared to the full-depth case $H/h=1$. For the former case, figure 6(a) indicates that both upstream and downstream pressure forces contribute to the drag decrease during the time interval $t/(h/V)\approx 3.3$–4.4. In contrast, for the full-depth case, $H/h=1$, the drag decrease is mainly due to an increasing downstream face pressure (cf. figure 10), while the variation of the upstream pressure force is small. In order to understand the reason for this discrepancy, it is instructive to analyse the flow-field evolution for the full-depth $H/h=1$ case (cf. figure 11). In the $t/(h/V)=3.9$ time frame, note the presence of both a wall recirculation region and a Kelvin–Helmholtz billow upstream of the cylinder. These flow structures remain almost stationary during the time interval $t/(h/V)\approx 3$–3.9 as the drag decreases. This explains the small variation of the upstream face pressure force during the interval $t/(h/V)\approx 3$–3.9. In contrast, as explained previously, upstream recirculation regions are convected vigorously towards the cylinder in the $H/h=5$ case as Kelvin–Helmholtz billows pass by, having a noticeable influence on the drag.

Figure 10 shows that the full-depth drag increases during $t/(h/V)\approx 3.9$–5.3. The $t/(h/V)=3.9$ frame of figure 11 indicates a continuous supply of vorticity from the cylinder top into the wake during this time interval, similar to the partial-depth case. In contrast to the partial-depth case, however, the full-depth case does not show the transport of vorticity from an upstream recirculation region into the wake. Thus the full-depth case experiences a less drastic drag fluctuation than the partial-depth case.

Data for the effect of H/h on the variation of the lift force F_L with time are shown in figure 9(b). Interestingly, the curves for all values of H/h track each other closely during the impact stage, so that the magnitude of the maximum lift force depends only weakly on H/h. However, the pronounced second lift maximum that we had observed for the partial-depth case is considerably weaker for the full-depth case. This reflects the reduced transport of concentrated vorticity patches past the top of the cylinder in the full-depth case, as described above.

3.4. *Effect of the Reynolds number*

The influence of the Reynolds number on the time-dependent drag force is displayed in figure 12(a). This figure shows that while the magnitude of the first maximum is

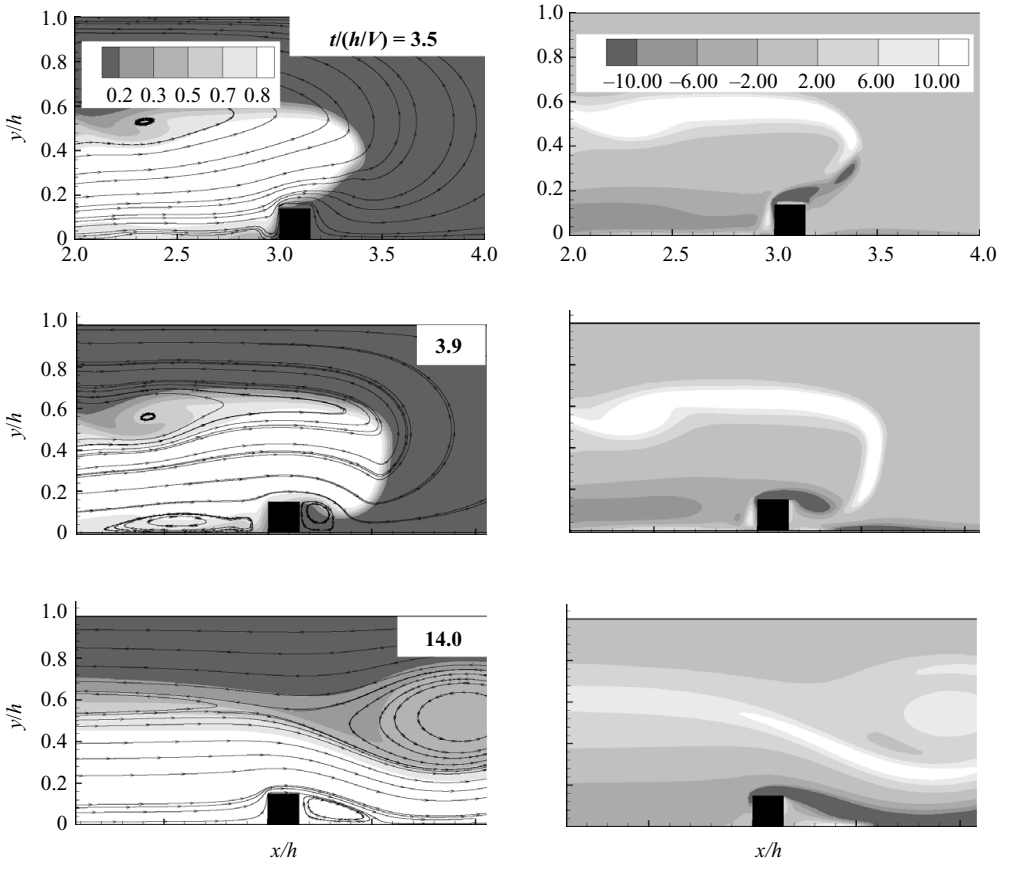

FIGURE 11. Temporal evolution of the concentration c^* (left) and the vorticity $\omega/(V/h)$ (right) fields as the gravity current interacts with the cylinder for the full-depth ($H/h = 1$) case.

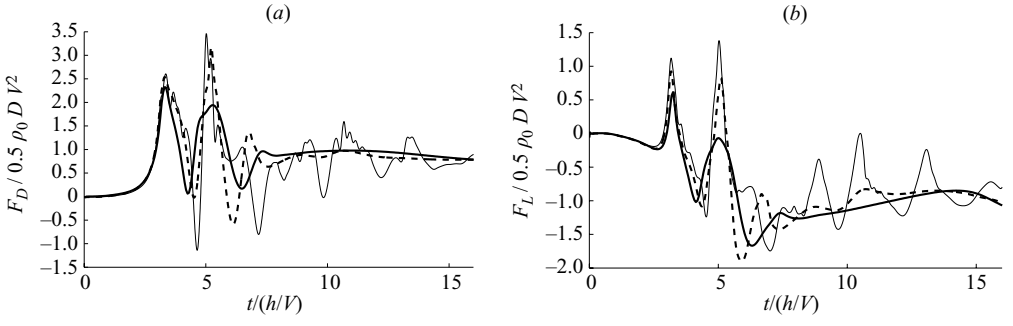

FIGURE 12. Effect of Re on drag (a) and lift (b) fluctuations in partial-depth $H/h = 5$ gravity currents: $Re = 2000$ (thick solid line), $Re = 4000$ (dashed line) and $Re = 10\,000$ (thin solid line). For higher Re values, the fluctuations are stronger and persist over longer times.

affected only weakly by Re, subsequent maxima and minima are more pronounced for higher Re values. Similarly, figure 12(b) shows an increase of lift fluctuations with Re. In the following, we will identify the reasons for the larger drag and lift fluctuations at higher Re values.

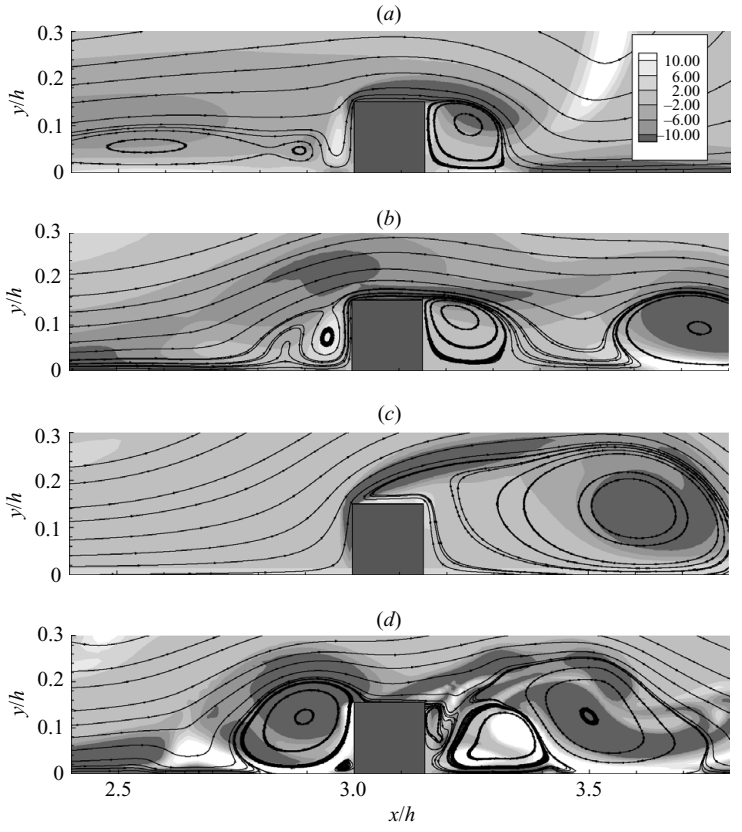

FIGURE 13. Instantaneous flow fields at the time of the first drag minimum for different simulations: (*a*) $H/h = 1$; (*b*) $H/h = 5$ (reference case); (*c*) $H/h = 5$ with slip bottom; (*d*) $H/h = 5$, $Re = 10\,000$. The grey shading denotes vorticity ($\omega/(V/h)$) contours. Streamlines highlight the upstream and downstream recirculation regions. Notice the absence of the upstream recirculation region in the case with a slip bottom boundary.

For the higher-Re case, the vorticity contours in figure 13 show more intense recirculation regions both upstream and downstream of the cylinder, at the time of the first drag minimum. Similar observations can be made at other times as well, consistent with the more pronounced force fluctuations at higher Re. Furthermore, for large Re these unsteady recirculation regions persist for longer times.

Figure 14 shows the temporal evolution of the drag for the $H/h = 5$ and $Re = 10^4$ case, along with the upstream and downstream pressure forces. Note that the drag fluctuations are dominated by the upstream face pressure force, suggesting that events upstream of the cylinder are responsible for the observed force fluctuations. The time interval between the drag minima shown in figure 14 is $\Delta t/(h/V) \approx 2.5$, which gives a frequency f of the force oscillations $f/(V/h) \approx 0.4$. An analysis of the lift data yields the same value for the dominant frequency.

Figure 15 shows the location of zero shear stress at the bottom wall as function of time, for the $Re = 2000$ and $Re = 10^4$ cases. The thick grey line indicates the cylinder position. This form of visualization allows us to study the formation and convection of recirculation regions in the vicinity of the cylinder. For $Re = 2000$, we observe a pair of recirculation regions propagating along the bottom wall towards the cylinder during

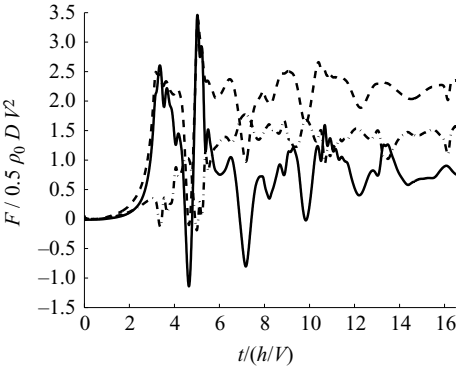

FIGURE 14. Temporal evolution of the drag for the $H/h = 5$ and $Re = 10^4$ case. Also shown are the pressure force F_w (dashed line) and F_e (dash-dotted line) on the upstream and downstream faces. The drag fluctuations are dominated by the pressure force on the upstream face.

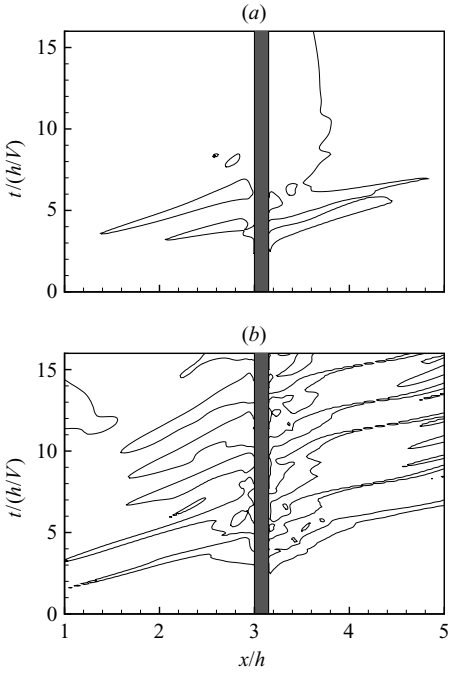

FIGURE 15. Location of zero shear stress at the bottom wall for the partial-depth $H/h = 5$ cases with $Re = 2000$ (a) and $Re = 10^4$ (b). The thick grey line denotes the location of the cylinder. The periodic formation and subsequent propagation of recirculation regions is sustained for longer times at larger Re values.

the time interval $t/(h/V) \approx 3$–6.5. No additional recirculation regions form thereafter. On the other hand, for $Re = 10^4$ the formation and convection of recirculation regions along the bottom wall is sustained for much longer times. The figure indicates that these near-wall recirculation regions are generated at time intervals of $\Delta t/(h/V) \approx 2.5$, which suggests that they are primarily responsible for the drag fluctuations described above.

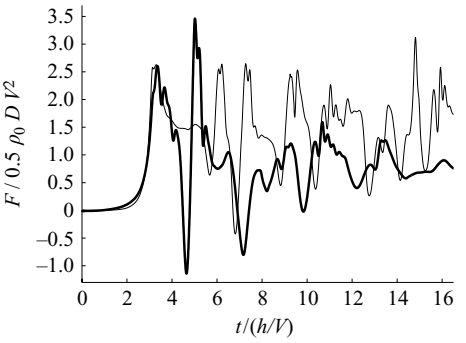

FIGURE 16. Effect of H/h on the total drag variation with time for $Re = 10\,000$: $H/h = 1$ (thin solid line), 5 (thick solid line).

Earlier observations by Härtel *et al.* (2000) for gravity currents without submerged cylinders had shown that the formation of recirculation regions along the bottom wall is closely linked to the Kelvin–Helmholtz billows in the interfacial region. An analysis of the flow field in the presence of a cylinder, for the reference case of $H/h = 5$ and $Re = 2000$, confirms this scenario. Figure 15(*a*) shows that the flow first separates at $t/(h/V) \approx 3$ and $x/h = 2$. From figure 2 we see that at this time a Kelvin–Helmholtz billow is located near $x/h = 1.6$. The fluid right underneath this billow is accelerated in the streamwise direction but subsequently slows down as it encounters an adverse pressure gradient. This, in turn, leads to the separation of the flow from the bottom wall and to the formation of a recirculation region. Hence, the existence of this recirculation region is due to a vortex-induced separation process (Doligalski, Smith & Walker 1994).

We now revisit the effect of the channel depth (H/h) for a higher Reynolds number. Figure 16 shows that for $Re = 10\,000$ the initial fluctuation of the drag in the interval $t/(h/V) \approx 3.3$–5 is stronger in partial-depth $H/h = 5$ currents than in full-depth $H/h = 1$ currents, just as we had observed earlier for $Re = 2000$ (cf. figure 9*a*). The mechanism of this initial drag fluctuation is the same at both Reynolds numbers. In contrast to lower Re values, however, the vortical structures upstream of the cylinder in full-depth, high-Re currents are no longer stationary by $t/(h/V) \approx 5.5$. Instead, they are convected towards the cylinder. In this way, they produce the drag fluctuations shown in figure 16, in the same manner as previously seen for partial-depth $H/h = 5$ currents. Figure 16 also shows that for $t/(h/V) > 7$ the drag fluctuations are larger in full-depth currents; the same was observed for the lift. These stronger fluctuations in full-depth currents are the result of more intense Kelvin–Helmholtz vortices at the interface between the two fluids. These vortices are stronger in full-depth currents because of the larger velocity difference between the two currents.

3.5. *Effect of a slip bottom boundary*

The importance of recirculation regions approaching the cylinder from upstream is further supported by figure 17, which analyses the effect of the bottom boundary condition on the drag for a partial-depth current. We note that the gravity-current front speed V (rather than u_b) is used as the velocity scale, to account for the fact that the front speed for the slip case is about 20 % higher than for the no-slip case (cf. table 2). While the maximum and the quasi-steady state drags are seen to depend only weakly on the bottom boundary condition, the drag decrease after the first maximum is noticeably reduced in the slip case. Figure 17(*b*) indicates that this is a result of

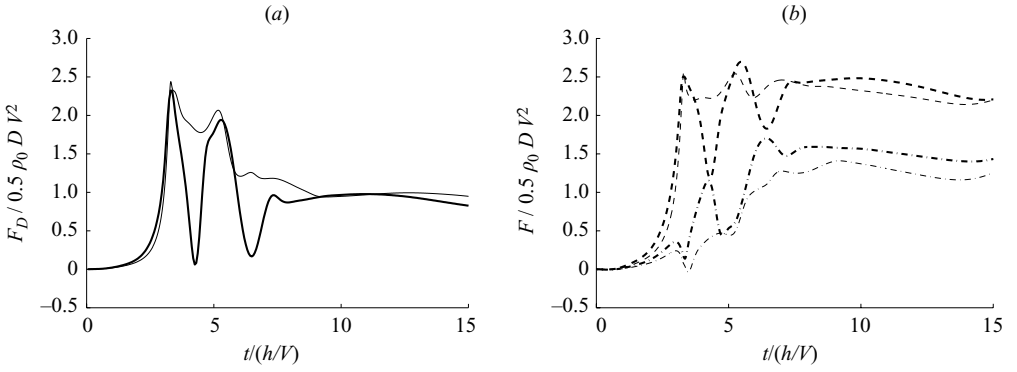

FIGURE 17. Effect of a no-slip (thick lines) or slip (thin lines) bottom boundary condition on the temporal evolution of the (*a*) drag and (*b*) pressure forces at the upstream (dashed line) and downstream (dash-dotted line) faces of the cylinder, in partial-depth $H/h = 5$ gravity currents. The initial drag fluctuation is noticeably reduced for the case with a slip bottom, as a result of weaker fluctuations in both the upstream and downstream pressure forces. This confirms that the formation and propagation of an upstream recirculation region for a no-slip bottom boundary strongly influences the drag.

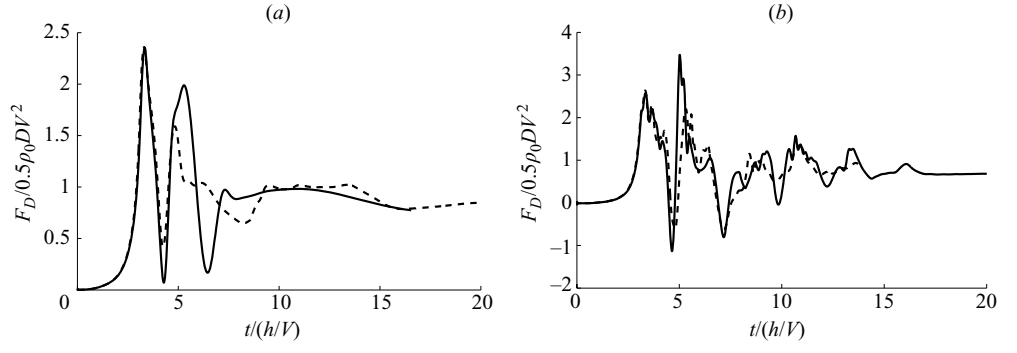

FIGURE 18. Effect of Sc on the drag variation with time in partial-depth $H/h = 5$ gravity currents at (*a*) $Re = 2000$ and (*b*) $Re = 10\,000$: $Sc = 1$ (solid line); $Sc = 10$ (dashed line).

weaker fluctuations in both the upstream and downstream pressure forces. Here, the weaker fluctuation of the upstream pressure force in the slip case reflects the absence of a recirculation region approaching from upstream (cf. figure 13). On the other hand, the downstream pressure fluctuations are reduced in the slip case because the wake recirculation region remains attached to the cylinder, rather than being swept downstream.

3.6. *Effect of the Schmidt number*

Figure 18 shows the effect of Sc on the drag variation with time for currents with $H/h = 5$ and (*a*) $Re = 2000$ and (*b*) $Re = 10\,000$. The effect of Sc is negligible during the impact stage ($t/(h/V) < 3.3$) and small at late times during the quasi-steady stage. The main effect of Sc manifests as a decrease of the drag fluctuation during $t/(h/V) = 4.2$–6.5, when Sc is increased from 1 to 10. Similar observations are seen for the lift.

4. Results from three-dimensional simulations

In this section we describe results from three three-dimensional LESs. The first simulation reproduces an existing experimental configuration, and its results will be compared to laboratory measurements. Subsequent three-dimensional simulations serve to establish the range of validity of two-dimensional simulations, along with the influence of the Reynolds number. Based on these simulations, we discuss the three-dimensional flow structures that form in the vicinity of the cylinder and their effect on the overall drag and its spanwise variation.

4.1. *Comparison with experiments*

In order to reproduce the experimental conditions of Ermanyuk & Gavrilov (2005*a*), a configuration similar to that depicted in figure 1 is employed but with a rectangular cylinder of height $D = 0.25h$ and width $W = 0.125h$ Furthermore, in following the experiments a gap of $0.0625h$ is left between the bottom wall and the cylinder bottom face. While this very narrow gap has a relatively small influence on the structure of the flow field, its presence is nevertheless required for the evaluation of lift data that can be compared with experimental values. Other parameter values are $L/h = 40$, $l/h = 20$, $H/h = 1.25$, $Re = 7084$ and $Sc = 10$. The domain length in the spanwise direction is $1.25h$. For comparison purposes, a two-dimensional simulation is carried out for this configuration as well, with a 2520×256 grid, while $2520 \times 256 \times 50$ points are used in the three-dimensional simulation. The above parameter values represent the experimental data set of Ermanyuk & Gavrilov (2005*a*) with the lowest value of the cylinder height to lock height ratio, so that this ratio lies within the range for D/h discussed earlier.

Even though the value of Sc chosen for the simulations is two orders of magnitude less than in the experiments, the values of Pe in both simulations ($O(10^4)$) and experiments ($O(10^6)$) are sufficiently high for the effects of diffusion on the dynamics of the interaction to be negligible, as will be evident later. In the experiments and the two-dimensional simulation, the rectangular region between $x = -l$ and $x = 0$ and between $y = h$ and $y = H$ (cf. figure 1) is filled with lighter fluid. On the other hand, in the three-dimensional simulation this region is taken to be a solid. This difference in the simulation approach has a negligible effect on the dynamics of the current, as the front speed varies by less than 2 % between the two- and three-dimensional simulations. Furthermore, the structure of the gravity-current head, and of the region upstream of it, was seen to be qualitatively very similar in the experiments and in the three-dimensional simulation. The experiments employ a channel whose width is approximately one order of magnitude larger than the rectangular cylinder height, so that the end effects should be negligible. The three-dimensional simulations reproduce this situation by using periodic boundary conditions in the spanwise direction. Following the approach of Ooi *et al.* (2007), three-dimensionality is triggered by means of small random disturbances in the initial conditions.

Figure 19 shows the evolution of the flow field by means of the $c^* = 0.1$ isosurface. The highly three-dimensional flow structures resulting from spanwise variations of the Kelvin–Helmholtz vortices, and from the lobe-and-cleft instability of the current front, are visible in figure 19(*a*), at a time before impact.

Figure 20 shows the temporal evolution of the spanwise-averaged drag and lift obtained from the two- and three-dimensional simulations and from the experiments by Ermanyuk & Gavrilov (2005*a*). Only the pressure components of the drag and lift calculated from the simulations are shown in figure 20 and in the remaining figures of § 4, as the viscous components are negligible. The exact distance between the lock

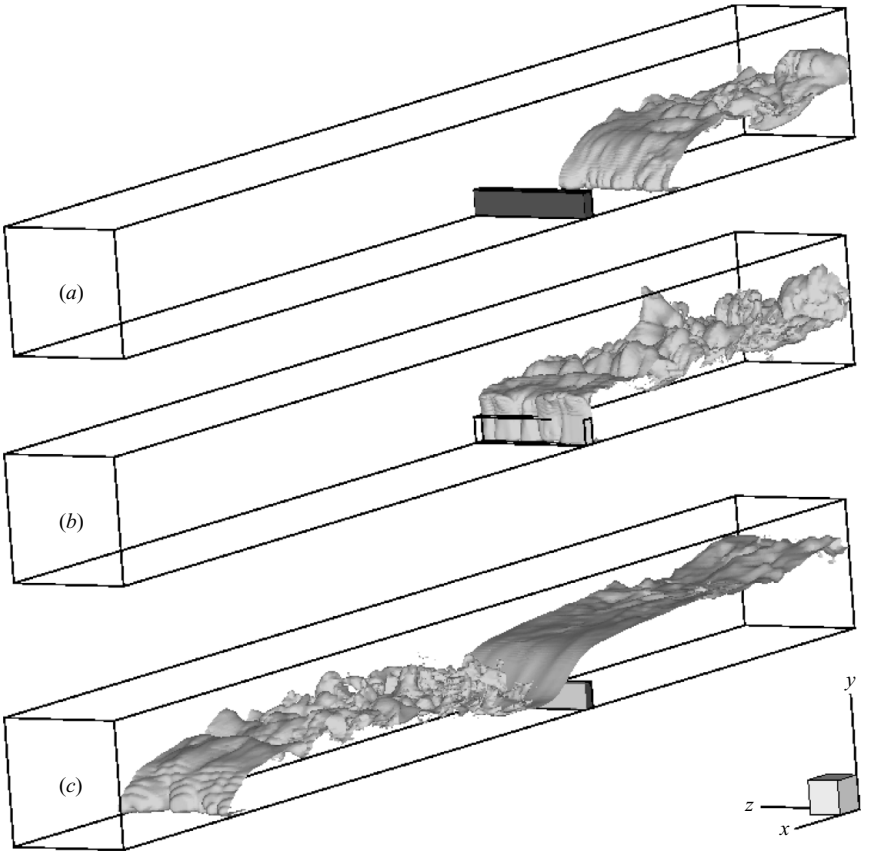

FIGURE 19. Temporal evolution of the flow field in a three-dimensional simulation with $H/h = 1.25$, $Re = 7084$ and $Sc = 10$. The concentration isosurface $c^* = 0.1$ is shown at $t/(h/V) = 5.78$ (a), 7.35 (b) and 14.7 (c). Note the gravity current's lobe-and-cleft structure in (a). The cylinder is outlined with wireframes in (b) to highlight the front structure during impact.

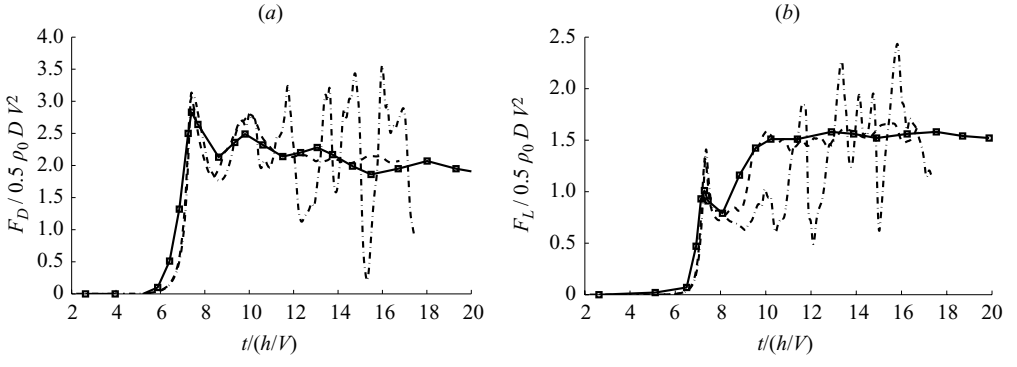

FIGURE 20. Temporal evolution of the drag (a) and lift (b) in the experiments by Ermanyuk & Gavrilov (2005a) (solid line, squares), the three-dimensional simulation (dashed line) and the two-dimensional simulation (dash-dotted line). While the three-dimensional simulation results compare well with experimental measurements, the two-dimensional simulation overpredicts the force fluctuations.

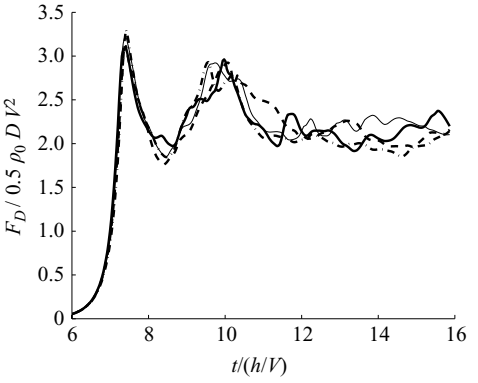

FIGURE 21. Temporal variation of the drag at different spanwise locations from the three-dimensional simulation for $H/h = 1.25$, $Re = 7084$ and $Sc = 10$: $z/h = 0.25$ (thick solid line), $z/h = 0.5$ (dashed line), $z/h = 0.75$ (dash-dotted line) and $z/h = 1$ (thin solid line).

gate and the cylinder l_c/h is not provided in Ermanyuk & Gavrilov (2005*a*) and is approximated here by using the front speed of the current and the time of maximum drag given in the experiments, which gives $l_c/h = 7.125$. Furthermore, in order to facilitate the comparison, the experimental curves in figure 20 are shifted along the abscissa so that the first drag maximum occurs at identical times in the experiment and the simulations.

Figure 20 demonstrates good overall agreement between the experimental results and those of the three-dimensional simulation. This confirms the negligible effect of Sc and of the slightly different flow configuration used in the three-dimensional simulation. A noticeable difference in figure 20(*b*) concerns the maximum lift value at $t/(h/V) = 7.35$, with a value of 1.32 in the simulations and 1 in the experiments. The likely cause for this difference lies in the low data-sampling rate of the experiments during impact. As pointed out by a referee, the force gauges employed in the experiments by Ermanyuk & Gavrilov (2005*a*) likely can resolve only time scales of about $\delta t = 0.12s$ or larger, which corresponds to a dimensionless value of 0.1. Hence, they may have slightly underestimated the very sharp first peak.

4.2. *Range of validity of two-dimensional simulations*

Figure 20 shows that throughout the impact stage, up to $t/(h/V) = 7.35$, the two-dimensional simulation results closely reproduce their three-dimensional counterparts. Hence the initial force variations are dominated by the two-dimensional mechanisms described in § 3.3, although, as we will see below, some spanwise drag variation exists during this interval. For $t/(h/V) > 10$, the two-dimensional simulation overpredicts the force fluctuations, indicating that three-dimensional flow features become important during this stage.

Figure 21 indicates that in the three-dimensional flow the temporal drag variations at each individual spanwise location are smaller than in the corresponding two-dimensional flow. The spanwise differences between local drag values are relatively minor. Hence the lower global drag fluctuations observed in the three-dimensional simulation are not simply a consequence of the spanwise integration but rather reflect a qualitatively different flow structure. This is confirmed by figure 22, which compares the spanwise vorticity fields from the two- and three-dimensional simulations during the quasi-steady state. Note that the strong and coherent Kelvin–Helmholtz vortices visible in the two-dimensional simulation are largely absent in the three-dimensional

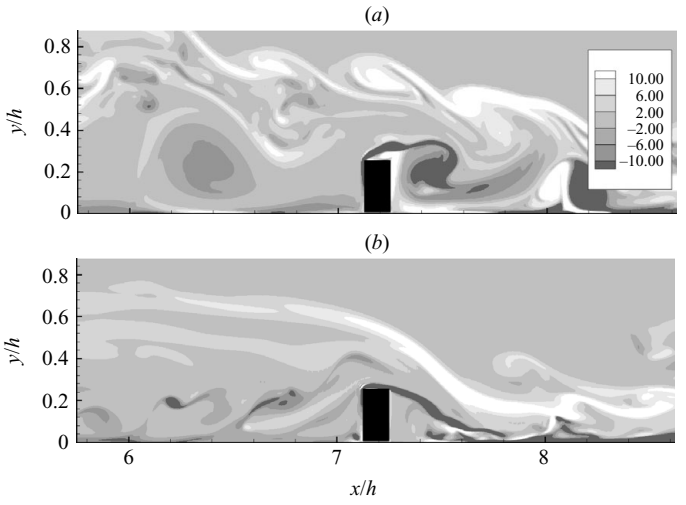

FIGURE 22. Comparison of the instantaneous spanwise vorticity field ($\omega_z/(V/h)$) at $t/(h/V) = 15.44$ during the quasi-steady state between the two-dimensional (a) and three-dimensional (b) simulations for $H/h = 1.25$, $Re = 7084$ and $Sc = 10$. The $z/h = 0.625$ middle plane is shown in (b).

flow. This is consistent with earlier observations for gravity-current flows without obstacles (e.g. Härtel *et al.* 2000; Ooi *et al.* 2007).

Section 3.4 had identified the impact of vortical structures propagating along the bottom wall as the main source of the two-dimensional drag fluctuations. These vortical structures owe their existence to strong, coherent Kelvin–Helmholtz vortices in the mixing layer. In three-dimensional flows, these Kelvin–Helmholtz vortices are significantly less coherent, so that the recirculation regions along the wall are less pronounced, which in turn reduces the drag fluctuations. We remark that this reason for the lower drag fluctuations in three dimensions is fundamentally different from what has been observed in constant-density flows past cylinders far away from walls. There the larger drag fluctuations predicted by two-dimensional simulations result from vortices that shed more closely to the cylinder (e.g. Mittal & Balachandar 1995).

Figure 23 shows the temporal evolution of the spanwise-averaged drag and lift obtained from two- and three-dimensional simulations with the same parameters as the reference case except $Re = 10\,000$, $L/h = 28$, $l/h = 12$ and $l_c/h = 9$. The longer distance between the gate and the cylinder, $l_c/h = 9$ instead of 3, is required to let the Kelvin–Helmholtz vortices break up and the lobe-and-cleft structure evolve. A grid of $1200 \times 300 \times 50$ (1200×300) is used in the three-dimensional (two-dimensional) simulation. The domain length in the spanwise direction is h. The small effect of l_c/h on the temporal evolution of the forces in the two-dimensional simulations is reflected by the corresponding curves in figures 23 and 12. Note that the two-dimensional simulation in figure 23 accurately captures the temporal force variation during impact ($t/(h/V) < 9$), while it overpredicts subsequent fluctuations. Again, this overprediction can be traced to the more coherent Kelvin–Helmholtz vortices in the two-dimensional simulation (from data not shown here). Thus, the observations on the effect of three-dimensionality on the force fluctuations made earlier in this section for the experimental configuration of Ermanyuk & Gavrilov (2005*a*) are also applicable

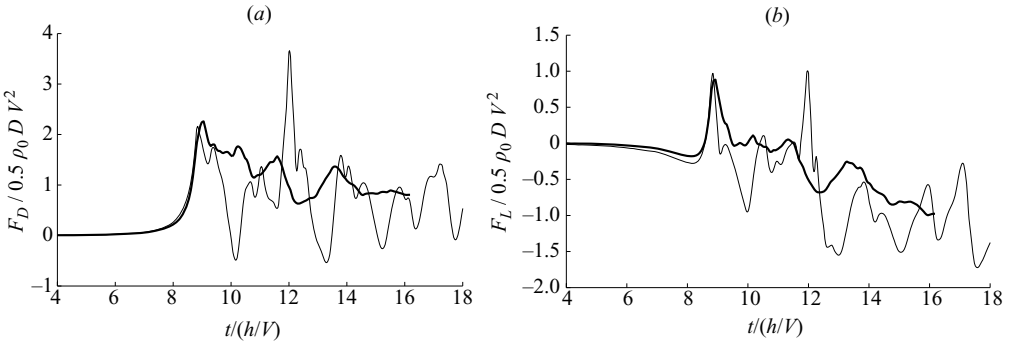

FIGURE 23. Temporal evolution of the drag (a) and lift (b) from two-dimensional (thin lines) and three-dimensional (thick lines) simulations with the parameters of the reference case, except $Re = 10\,000$, $L/h = 28$, $l/h = 12$ and $l_c/h = 9$. The two-dimensional simulation reproduces the time-dependent forces during impact ($t/(h/V) < 9$), while it overpredicts the subsequent fluctuations.

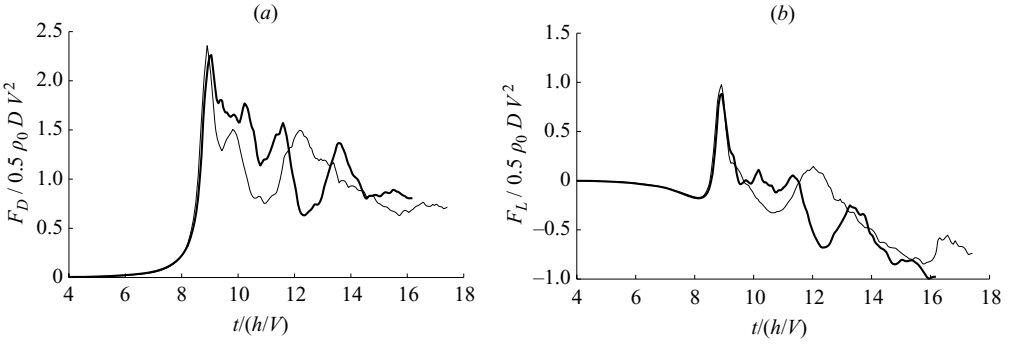

FIGURE 24. Temporal evolution of the spanwise-averaged drag (a) and lift (b) from three-dimensional simulations for $Re = 10\,000$ (thick lines) and $Re = 50\,000$ (thin lines) and the parameters of the reference case, except $L/h = 28$, $l/h = 12$ and $l_c/h = 9$. An increase of Re from 10 000 to 50 000 does not have a strong effect on the magnitude of the force fluctuations.

for flows without a gap between the wall and the cylinder and for parameter values comparable to those considered in § 3.

4.3. *Effect of the Reynolds number*

Figure 24 shows that an increase of Re from 10 000 to 50 000 has a relatively small effect on the magnitude of the force fluctuations. This finding represents an important result, as it suggests that lower-Re simulations can make useful predictions for applications involving high-Re gravity currents.

We now compare the temporal evolution of the flow field, along with the associated drag and pressure forces at the faces of the cylinder, for the reference case and the three-dimensional simulation at $Re = 50\,000$. A comparison of figures 6(a) and 25 shows that in both cases a similar increase of F_w results in the first drag maximum when the gravity current impinges on the cylinder (cf. figures 4 and 26a). Furthermore, similar fluctuations of F_w and F_e lead to the drag variation between its first and second maximum. In the two cases compared here, these fluctuations of F_w and F_e are seen to occur as Kelvin–Helmholtz billows pass by the cylinder, and patches of negative vorticity are convected towards the cylinder. These billows and vorticity patches take

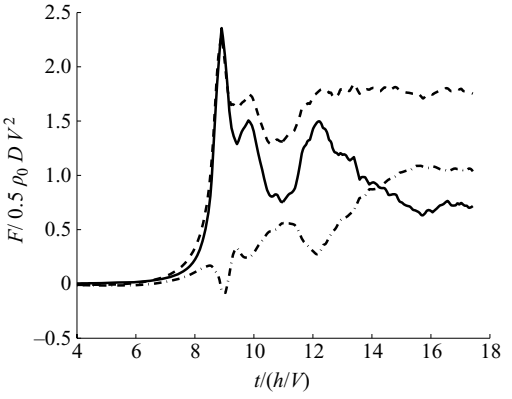

FIGURE 25. Temporal evolution of the spanwise-averaged drag from the three-dimensional simulation at $Re = 50\,000$ and the parameters of the reference case, except for $L/h = 28$, $l/h = 12$ and $l_c/h = 9$. Also shown are the spanwise-averaged pressure forces F_w (dashed line) and F_e (dash-dotted line) on the upstream and downstreamfaces.

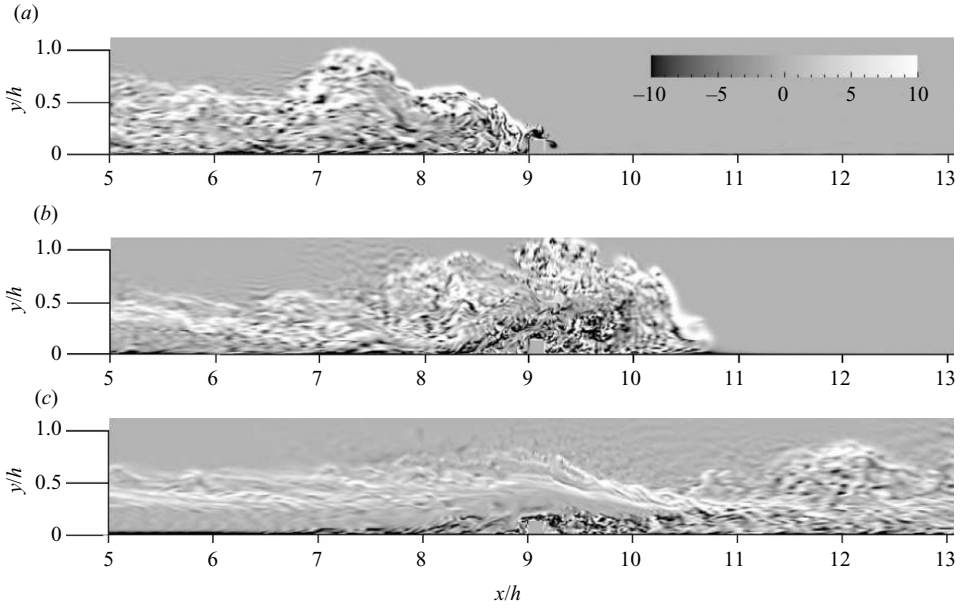

FIGURE 26. Spanwise vorticity $\omega_z/(V/h)$ fields at $z/h = 0.5$ and at different times, from the three-dimensional simulation at $Re = 50\,000$ and the parameters of the reference case, except $L/h = 28$, $l/h = 12$ and $l_c/h = 9$: (*a*) $t/(h/V) = 8.8$; (*b*) $t/(h/V) = 10.9$; and (*c*) $t/(h/V) = 17.2$.

the form of strong coherent vortical structures in the two-dimensional low-Re reference case (cf. figure 4), while they are somewhat more intermittent in the three-dimensional $Re = 50\,000$ case (cf. figure 26*b*). In this figure, the centre of a Kelvin–Helmholtz billow is located at $x/h \approx 8$ and $y/h \approx 0.5$. Figures 6(*a*) and 25 show that the drag reaches a quasi-steady value later on. In the two cases considered here, the wake during the later quasi-steady stage is distorted by the dense fluid downstream of the cylinder (cf. figures 4 and 26*c*). Similar observations hold for the temporal evolution of the lift (cf. figures 6*b* and 23*b*). Note that the force fluctuations during the transient

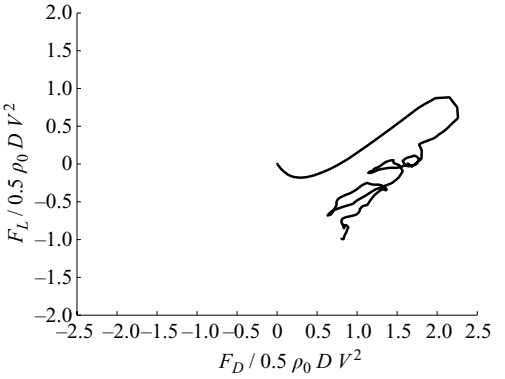

FIGURE 27. Hodograph of the tip of the force vector from the three-dimensional simulation at $Re = 50\,000$ and the parameters of the reference case, except $L/h = 28$, $l/h = 12$ and $l_c/h = 9$.

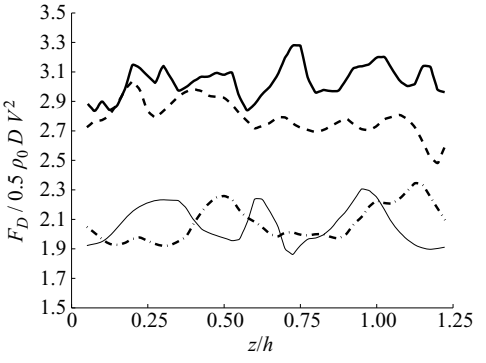

FIGURE 28. Spanwise variation of the drag at different times, from a three-dimensional simulation with $H/h = 1.25$, $Re = 7,084$ and $Sc = 10$: $t/(h/V) = 7.35$ (first drag maximum, thick solid line), $t/(h/V) = 10$ (second drag maximum, dashed line), $t/(h/V) = 13.12$ (dash-dotted line), $t/(h/V) = 14.7$ (thin solid line).

stage are larger in the reference case, as can be seen by comparing the hodographs in figures 8 and 27. Interestingly, the flow processes leading to the force fluctuations in the high-Re, three-dimensional simulations are qualitatively more similar to those seen in two-dimensional simulations at lower Re than at equivalent Re.

4.4. *Spanwise variation of the drag and associated flow structures*

We now discuss the spanwise variation of the drag and associated flow structures, based on results from a three-dimensional simulation with $H/h = 1.25$, $Re = 7084$ and $Sc = 10$. Figure 28 shows spanwise peak-to-peak variations of the local drag up to 20 %. A detailed analysis indicates that these variations are mainly due to spanwise pressure differences on the upstream face of the cylinder (F_w). This is in contrast to constant-density flows past cylinders far away from walls, in which the spanwise variation of the drag is determined by flow structures in the wake. Consequently, the following discussion will focus on the flow upstream of the cylinder.

The typical lobe-and-cleft structure of the gravity-current front is visible in figure 19(*a*). The temporal evolution of this structure during the time interval $t/(h/V) = 5.78$–7.35 is visualized by means of $c^* = 0.1$ contours in the $y/h = 0.0025$ plane in figure 29. Note the continuous merging and splitting of the lobes as the

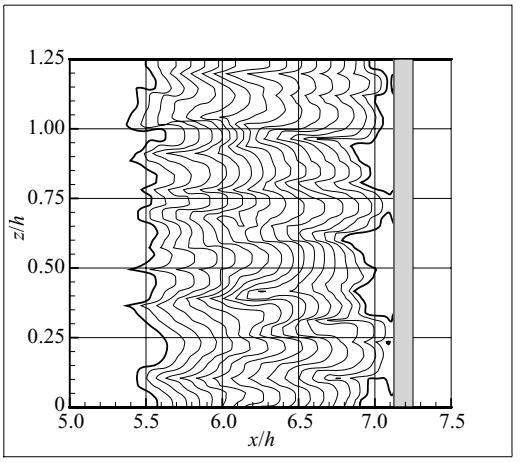

FIGURE 29. Temporal evolution of the lobe-and-cleft structure before impact, from a three-dimensional simulation with $H/h = 1.25$, $Re = 7084$ and $Sc = 10$. Concentration $c^* = 0.1$ isolines at the $y/h = 0.0025$ plane in the interval $t/(h/V) = 5.78$–7.35 right before impact are shown. The isolines at $t/(h/V) = 5.78$ and 7.35 are denoted with thick solid lines. The position of the cylinder at $x/h = 7.125$–7.25 is indicated by a grey bar.

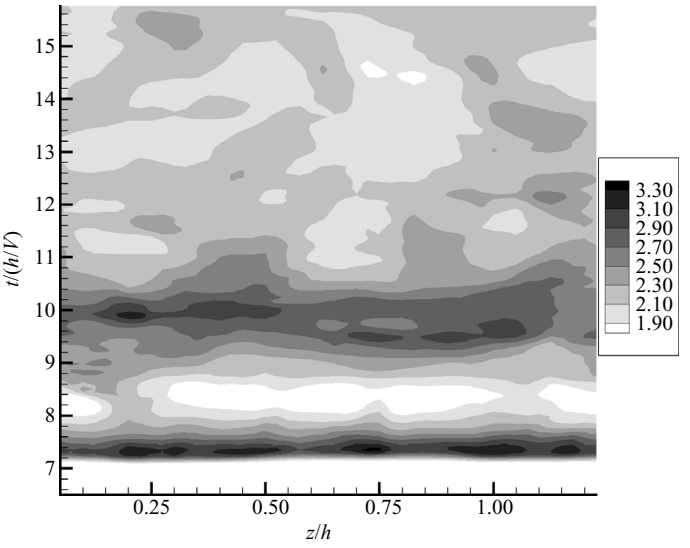

FIGURE 30. Evolution of the spanwise variation of the drag ($F_D/0.5\rho_0 DV^2$) with time, from a three-dimensional simulation with $H/h = 1.25$, $Re = 7084$ and $Sc = 10$. The spanwise length scale increases with time.

current approaches the cylinder. A comparison of figures 28 and 29 shows that at $t/(h/V) = 7.35$ those locations at which the lobes make contact with the cylinder correlate well with the locations of maximum drag. During the quasi-steady stage, the length scale of the spanwise drag variation increases, as compared to the impact stage (cf. figure 28). This suggests that the flow structure upstream of the cylinder changes as the current transitions from the impact to the quasi-steady stage. The effect of this unsteady flow structure on the spanwise drag variation and its characteristic length scale is visible in figure 30. Thus, while during impact the length scale of the spanwise

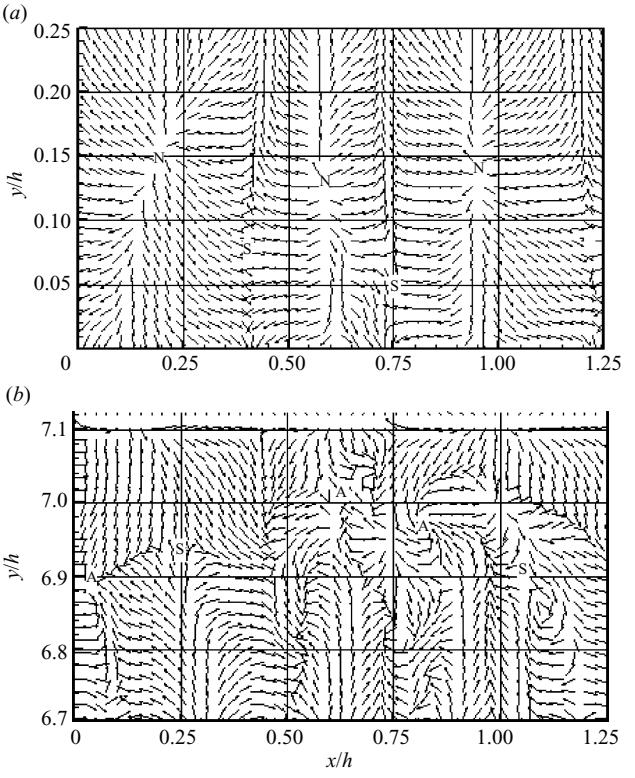

FIGURE 31. Instantaneous velocity direction vectors on the upstream face of the cylinder (*a*), and at the bottom wall immediately upstream of the cylinder (*b*) during the quasi-steady state at $t/(h/V) = 14.7$, from a three-dimensional simulation with $H/h = 1.25$, $Re = 7084$ and $Sc = 10$. The cylinder height is $0.25h$ and its upstream face is located at $x/h = 7.125$. The approximate locations of repelling nodes (N), saddles (S) and attracting nodes (A) are shown.

drag variation is set by the front's lobe-and-cleft structure, during the quasi-steady stage a different unsteady flow structure determines the spanwise drag variation. This flow structure is to be described next.

Figure 31 displays instantaneous velocity direction vectors (*a*) on the upstream face of the cylinder and (*b*) at the bottom wall immediately upstream of the cylinder, at a time during the quasi-steady state. A pattern of repelling nodes (N) and saddles (S) can be recognized along the upstream cylinder face, while attracting nodes (A) and saddles (S) exist at the bottom wall. A comparison of figure 31(*a*) with the $t/(h/V) = 14.7$ curve of figure 28 shows that the drag peaks occur approximately at the node locations, where fluid impinges on the cylinder.

A further important characteristic of the flow structure, not shown here, is the presence of recirculation regions immediately upstream of those locations at which nodes exist along the upstream cylinder face. One way of visualizing the flow structure upstream of the cylinder is shown in figure 32, by means of vorticity magnitude contours ($\sqrt{\omega_i\,\omega_i}/(V/h)$).

The flow features upstream of the cylinder are qualitatively similar to those observed in constant-density flows past bottom-mounted square cylinders (Martinuzzi & Tropea 1993 and Kim & Lee 2001). An idealized form of this type of cellular structure is depicted in figure 33, which has been adapted from Martinuzzi & Tropea (1993).

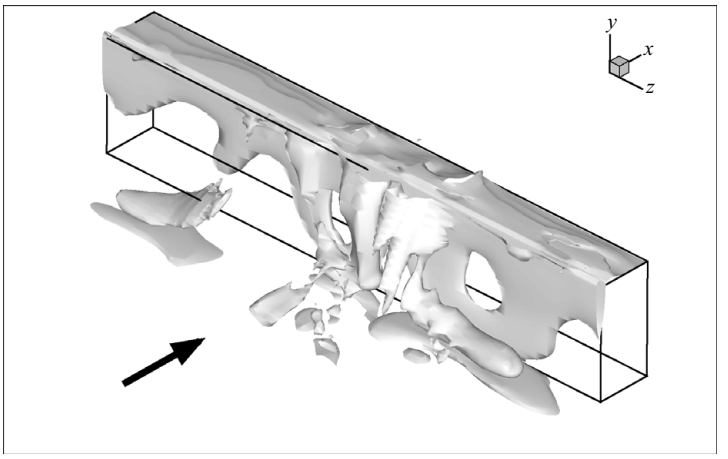

FIGURE 32. Flow structure upstream of the cylinder at $t/(h/V) = 14.7$, from a three-dimensional simulation with $H/h = 1.25$, $Re = 7084$ and $Sc = 10$. A contour of the vorticity magnitude ($\sqrt{\omega_i\,\omega_i}/(V/h)$) in the vicinity of the cylinder is shown, together with wireframes indicating the position of the cylinder.

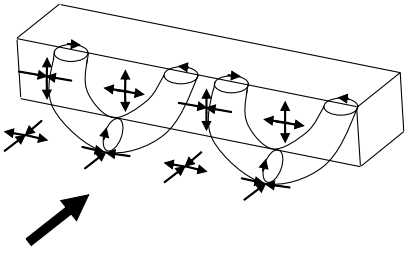

FIGURE 33. Idealized model of the flow structure upstream of the cylinder. Adapted from Martinuzzi & Tropea (1993).

These structures result in the spanwise non-uniformity of the flow and in preferred flow paths over the cylinder (Martinuzzi & Tropea 1993; Kim & Lee 2001).

5. Analysis of the force during the impact stage

5.1. *Maximum drag and lift amplitude*

As seen in figure 6, at $Re = 2000$ the drag and lift vary most strongly during the impact and transient stages. We will now discuss the effect of the various flow parameters on the maximum drag $F_{D,max}$ and the lift amplitude $F_{L,amp}$. This discussion will be based on results from two-dimensional simulations, since they accurately capture this stage, as discussed in § 4. We define the maximum drag as the first peak in the drag versus time curve, which occurs approximately when the current meets the cylinder. The lift amplitude is defined as the difference between the first maximum and the first minimum of the lift versus time curve.

Since $F_{D,max}$ depends on ρ, D, H, h, V, g' and μ, Buckingham's Π-theorem yields

$$\frac{F_{D,max}}{\frac{1}{2}\rho_0 D V^2} = f\left(\frac{D}{h}, \frac{H}{h}, \frac{V}{u_b}, Re\right). \tag{5.1}$$

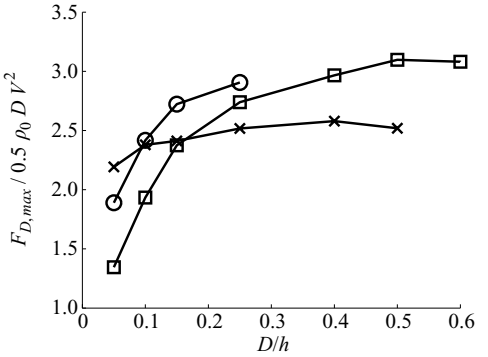

FIGURE 34. Effect of D/h on the maximum drag for the reference case (squares), the reference case with a slip bottom (crosses) and the reference case with $Re = 50\,000$ (circles).

A corresponding relationship holds for $F_{L,amp}$. As discussed previously, the lock height h represents a measure of the gravity-current height, since the latter is approximately $h/2$.

Figure 34 illustrates the effect of D/h on the maximum drag $F_{D,max}/0.5\rho_0 DV^2$ for the reference case, the reference case with a slip bottom wall and the reference case with $Re = 50\,000$. To save computational effort, the $Re = 50\,000$ data had to be obtained for a shorter domain with $L/h = 13$, $l/h = 6$, $l_c/h = 3$ and a grid of 2800×800 points. Note that the maximum drag increases with D/h in the range $D/h = 0.05$–0.4 and subsequently plateaus in the range $D/h = 0.4$–0.6. In order to interpret this result, it is helpful to define a boundary layer thickness δ_{90}, at which the time-averaged horizontal velocity reaches 90 % of its maximum. For gravity currents with $Re = 2000$ (50 000), we find that $\delta_{90}/h \approx 0.14$ (0.02). Thus, as long as D is $O(\delta_{90})$, the dimensionless drag increases with D/h. This suggests that the drag increase with D/h occurs because more of the cylinder is exposed to the larger velocity outside the boundary layer. This explanation is supported by the slip wall results in figure 34, which show the drag to increase much less in the absence of a viscous boundary layer. For a slip bottom wall, the moderate drag increase with D/h is primarily due to the blockage effect of the cylinder: a larger cylinder blocks more of the current, resulting in a larger maximum drag.

Note that the above scaling considerations would change when the cylinder is sufficiently large to completely block the current. While this case is not considered here, it has been observed by other authors that a complete blockage of the current occurs with cylinders whose height is at least twice the gravity-current height, i.e. $D/h \approx 1$ (Rottman *et al.* 1985; Lane-Serff *et al.* 1995). For these conditions, the drag should be scaled with the lock height h or with the current height, rather than with the cylinder height D.

For the reference case, figure 35 shows a slight increase of $F_{D,max}/0.5\rho_0 DV^2$ with Re. Since figure 6 had shown the viscous drag component to be negligible, the increase of the maximum drag with Re must be due to a decrease in the boundary layer thickness that exposes more of the cylinder to the free stream. However, note in figure 35 that the overall effect of Re is rather small, with an asymptotic value $O(2.7)$ being reached for large Re.

The effect of H/h on the maximum drag $F_{D,max}/0.5\rho_0 DV^2$ is shown in figure 36(a) for no-slip bottom walls with $D/h = 0.15$ and $D/h = 0.1$ and for a slip bottom wall with $D/h = 0.15$. Figure 36(b), which plots the same data against V/u_b, demonstrates

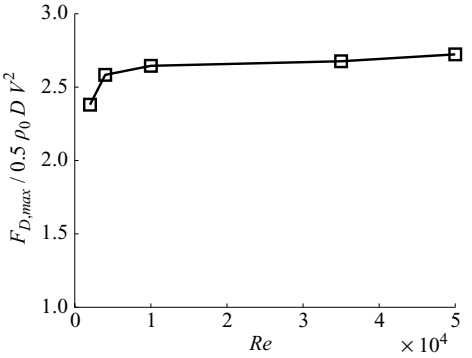

FIGURE 35. Effect of Re on the maximum drag during the impact stage, for the reference case.

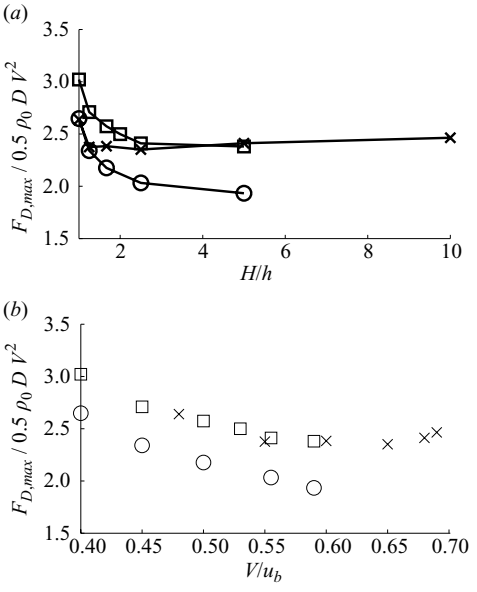

FIGURE 36. Effect of H/h (a) and V/u_b (b) on the maximum drag for no-slip bottom walls with $D/h = 0.15$ (squares) and $D/h = 0.1$ (circles) and for a slip bottom wall with $D/h = 0.15$ (crosses).

that the effect of varying H/h is primarily felt through the gravity-current front velocity V/u_b. Note the good collapse of the data for the no-slip and slip cases, which confirms V/u_b as the main parameter. This is remarkable, considering the strong effect of H/h on the flow field: While the upper layer of fluid moves upstream with very small velocities in the $H/h = 5$ case, it moves with a front speed approximately equal to that of the gravity-current front speed in the $H/h = 1$ case.

Figure 37 quantifies the effect of D/h on the (first) lift amplitude $F_{L,amp}/0.5\rho_0 DV^2$. As D/h increases, we observe (from data not shown here) stronger vertical velocities develop immediately upstream of the cylinder as more of the dense fluid is blocked. This reinforces the clockwise vortex above the cylinder, thereby increasing the upward suction. On the other hand, the effect of Re and H/h on the lift amplitude was found to be negligible. We remark that at higher Re the maximum lift amplitude does

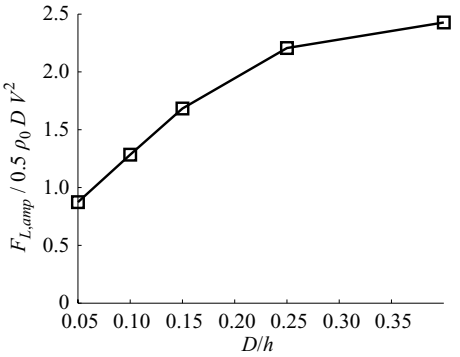

FIGURE 37. Effect of D/h on the maximum lift amplitude for the reference case.

not necessarily occur during the impact stage, similar to our earlier finding for the maximum drag.

5.2. *Upper bound for the maximum drag*

In order to derive an upper bound for the drag, consider an inviscid flow with $H \gg h$. At the time of maximum drag, when the gravity current of height $h/2$ is about to impinge on the square cylinder with side D, the hydrostatic pressure at $y = 0$ immediately upstream of the cylinder can be estimated as $\rho_0 g(H - h/2) + \rho_1 g h/2$. Its counterpart immediately downstream of the cylinder is $\rho_0 g H$. By applying these hydrostatic pressure values along the entire respective face, which would be valid for $D \ll h$, as occurs in practice, we obtain the hydrostatic component of the drag as

$$\frac{F_{D,hyd}}{\rho_0 D g' \frac{h}{2}} \approx 1. \tag{5.2}$$

The dynamic component of the drag can be bounded correspondingly. Since the wake flow downstream of the cylinder is quite weak, the dynamic drag component results mostly from the deceleration of dense fluid flow as it encounters the cylinder. Bernoulli's principle gives

$$\frac{F_{D,dyn}}{\frac{1}{2}\rho_0 D V^2} \approx 1. \tag{5.3}$$

An upper bound for the maximum drag can now be obtained by adding (5.2) and (5.3). For the reference case, with the front velocity V taken from the simulations, we obtain $F_{D,max}/0.5\rho_0 D V^2 \approx 3.9$. The case of $H/h = 5$ with a slip bottom gives a value of 3.16. A comparison of these values with the numerical results of figure 34 indicates an overprediction of the simulation data by about 30 %.

Figure 36(*b*) shows a roughly 20 % increase of the maximum drag $F_{D,max}/0.5\rho_0 D V^2$ as V/u_b decreases. This effect is qualitatively captured by the above upper bound, since (5.2) and (5.3) give $F_{D,max}/0.5\rho_0 D V^2 = 1 + (V/u_b)^{-2}$.

6. Comparison with constant-density flows

A comparison between the reference case and a similar, constant-density flow can be instructive in terms of providing insight into the dominant mechanisms. For this purpose, we conducted a two-dimensional simulation of constant-density flow around a square cylinder with side D, positioned at the bottom of a channel with length $60D$ and height $8D$. A no-slip (slip) condition is imposed at the bottom (top) wall, a

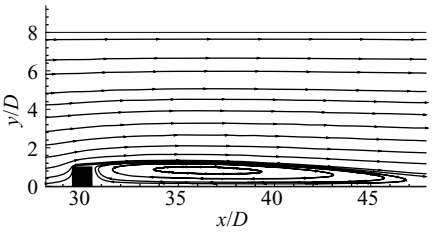

FIGURE 38. Instantaneous flow field for the constant-density flow past a bottom-mounted square cylinder at $Re_D = 177$.

uniform velocity V at the inlet and a convective outflow condition at the downstream boundary. A uniform Cartesian grid of size 1000×200 is employed.

The comparison is performed for $Re_D = 177$, which is sufficiently low for three-dimensional effects to be small and for the (near) wake to be steady in the constant-density flow. The boundary layer thickness (δ_{90}/D) at the cylinder location for the constant-density flow is about 0.8, which is close to the value of 0.9 for the reference case above.

The resultant flow field for the constant-density flow problem, shown in figure 38, yields a quasi-steady drag $F_D/0.5\rho_0 DV^2 = 0.63$. Note that this value is much lower than the corresponding value of 1.44 observed for a square cylinder far away from any wall at $Re_D = 150$ (Sohankar, Norberg & Davidson 1999). The lower value in the present case is due to the bottom wall, which suppresses vortex shedding and induces a boundary layer upstream of the cylinder.

The main difference between the gravity-current flow and its constant-density counterpart is the absence of an impact stage in the latter, as it does not involve the propagation of a front. However, even during the quasi-steady stage, significant differences exist between the two flows. A comparison of the $t/(h/V) = 11.8$ frame of figure 4 with figure 38 shows that the length and maximum width of the reference case wake are about $3.5D$ and D, respectively, and $18D$ and $1.25D$ in the constant-density flow problem. The corresponding values for the drag are $F_D/0.5\rho_0 DV^2 = 0.94$ and 0.63, respectively. Hence, the flow of dense fluid around the cylinder distorts the wake and increases the drag. A close inspection of the simulation data shows that the higher drag found in the reference case is mainly due to the presence of the hydrostatic drag component:

$$F_{D,hyd} = \int_A -n_x p_{hyd} \, \mathrm{d}A, \tag{6.1}$$

where n_x is the streamwise component of the outer normal n_i of the cylinder surface A, and the hydrostatic pressure is given by

$$p_{hyd} = \int_y^H \frac{c - c_0}{c_1 - c_0} \, \mathrm{d}y. \tag{6.2}$$

We find that for the reference case roughly one quarter of the total drag during the quasi-steady stage is due to the hydrostatic drag component, which is absent in the constant-density flow problem.

The analysis of the effects of D/h, H/h, Re and Sc (cf. figures 5, 9, 12 and 18) showed that D/h is the most influential parameter with respect to the drag during the quasi-steady stage. On the other hand, investigations of constant-density flows past cylinders near walls identify Re_D and δ_{90}/D as influential parameters (e.g.

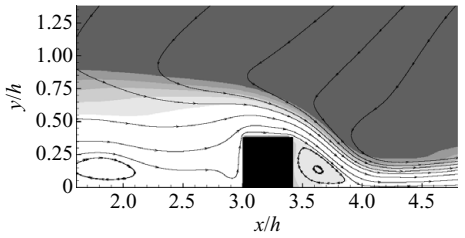

FIGURE 39. Instantaneous flow field for the $D/h = 0.4$ case at $t/(h/V) = 14.16$. Instantaneous streamlines are superimposed on the concentration (c^*) field.

Bearman & Zdravkovich 1978). This suggests that for gravity-current flows, the effect of D/h on the drag is felt through its influence on δ_{90}/D and Re_D. Of more importance, however, is the effect of D/h on the structure of the flow field around the cylinder during the quasi-steady state. A comparison of the $t/(h/V) = 11.8$ frame of figure 4 with figure 39 indicates that for the larger cylinder the upstream and downstream levels of the dense fluid are more disparate, which results in increased hydrostatic drag. Specifically, we found the ratio $F_{D,hyd}/F_D$ to be 5 % at $D/h = 0.05$, 25 % at $D/h = 0.15$, 45 % at $D/h = 0.4$ and 66 % at $D/h = 0.5$. Hence, the hydrostatic drag component is pivotal for the overall drag increase with D/h. For a further discussion of the hydrostatic drag based on hydraulic theory, cf. Baines (1995, p. 44).

It is also instructive to compare the present flow with the investigation by Castro (2002), who considered weakly stratified flow past a bottom-mounted flat plate inside a channel, with slip walls at the bottom and top boundaries. The level of stratification, given by the Richardson number, is sufficiently weak so that no internal waves are generated. For $Re_D = 100$, Castro (2002) shows that the drag $F_D/0.5\rho_0 DV^2$ decreases monotonically with increasing stratification, as long as internal waves are absent. With increasing stratification, the vertical velocity near the separation point – and thus the vorticity shed into the wake – are reduced, which in turn lowers the drag. By comparison, diffusion of baroclinically generated vorticity into the wake is less influential. In the present flow, stratification effects are mainly confined to the interface between the two fluids, while the density in the vicinity of the separation point is approximately constant (cf. the $t/(h/V) = 11.8$ frame of figure 4). Hence, drag reduction via the suppression of vertical velocities near the separation point is not observed.

7. Summary and conclusions

The present study has investigated the unsteady drag and lift forces to which a submarine, bottom-mounted square cylinder is subjected by an impinging gravity current. Towards this end, two- and three-dimensional, high-resolution Navier–Stokes simulations have been conducted that provide detailed information on the time-dependent pressure distributions along the surface of the cylinder, along with quantitative insight into the physical mechanisms generating these forces.

Two-dimensional simulations demonstrate that temporal force fluctuations are primarily caused by separated flow regions periodically approaching the cylinder from upstream. These flow regions are generated by Kelvin–Helmholtz vortices in the mixing layer between the gravity current and the ambient fluid. Increasing Reynolds numbers result in larger and more sustained force fluctuations due to more intense separated flow regions approaching the cylinder.

A comparison of two- and three-dimensional simulation results shows that the impact of the gravity current on the cylinder is essentially two-dimensional in nature. Thus, two-dimensional simulations can be used to explore this stage. However, beyond the impact stage and at high Re two-dimensional simulations noticeably overpredict the force fluctuations, due to unrealistically coherent Kelvin–Helmholtz vortices. Figure 12 suggests that unrealistic force fluctuations appear in two-dimensional simulations for Re values $O(10\,000)$ or higher.

The flow processes and their effects on the unsteady force observed in low-Re ($O(1000)$) two-dimensional simulations are qualitatively similar to those seen in high-Re ($O(10\,000)$) three-dimensional simulations. As a key difference, coherent vortical structures approach the cylinder from upstream during the transient stage in the former, while intermittent vorticity patches convect towards the cylinder in the latter. The similarities of the flow processes seen in low- and high-Re simulations, and the small effect of Re on the temporal evolution of the drag and lift seen in three-dimensional simulations, suggest that low-Re simulations can provide useful predictions for higher-Re flows.

At impact the gravity current's lobe-and-cleft structure sets the spanwise variation of the drag. Beyond impact, an unsteady cellular flow structure emerges upstream of the cylinder and produces a peak-to-peak variation of the drag of up to 20 %, with a characteristic length that scales with the cylinder height. This cellular structure is similar to that found in constant-density flows past bottom-mounted square cylinders.

The largest force magnitudes occur at impact, so that they can be studied via two-dimensional simulations. The ratio of cylinder height to current height represents an important geometrical parameter. Larger cylinders are seen to experience higher drag, as they are more exposed to the energetic high-speed core of the gravity current. Small cylinders, which are mostly submerged in the viscous boundary layer for no-slip bottom walls, see a larger drag in corresponding slip wall simulations, where a boundary layer does not form. Higher Reynolds numbers result in slightly larger drag forces, due to the thinner associated boundary layers.

A comparison of a gravity-current flow impinging on a bottom-mounted cylinder with a corresponding constant-density flow reveals several key differences. The impact stage, which requires the existence of a front, does not have a counterpart in constant-density flows. Furthermore, the hydrostatic drag component, absent in constant-density flows, is found to be important for gravity currents, especially for larger D/h. Finally, we observe that the downward motion of the dense fluid immediately downstream of the cylinder strongly influences the wake and thus the drag.

Recently, a preliminary design drag coefficient of 1.25 has been suggested for bottom-mounted submarine structures encountered perpendicularly by a gravity current (Bruschi *et al.* 2006). The uncertainty associated with this value, due to a lack of drag measurement data, is recognized by the authors. The present simulation results indicate that the drag coefficient reaches a peak near 3 at impact and later settles to a value of about 1. This information will be useful in the selection of a design drag coefficient for submarine structures under the potential impact of gravity currents. Our study also shows that because of the small torque the force vector can be assumed to act through the geometric centre of the structure. Furthermore, the force vector is directed downstream and upward when the current first meets the structure and downstream and downward during the later stages. This information will aid in the design of the aforementioned structures.

There are several directions in which the present investigation can be extended. Besides considering cylinders of different shapes, an interesting question concerns the

influence of a larger gap between the cylinder and the bottom wall. The presence of such a gap, which may form due to scouring in marine applications, might result in periodic vortex shedding from the cylinder, so that the issue of potential resonant interactions with the periodic separated flow regions approaching from upstream arises. Furthermore, it will be of interest to analyse the influence of a sloping bottom boundary (Birman *et al.* 2007) or of stronger density differences (Birman, Martin & Meiburg 2005; Lowe, Rottman & Linden 2005) on the current/cylinder interaction. Finally, the extension to depositing and eroding currents (Blanchette *et al.* 2005) is relevant to applications in which scour is a concern. Efforts to unravel these effects are currently underway.

The authors wish to acknowledge several helpful discussions with Ben Kneller and the help of Talia Ekin Tokyay with the three-dimensional simulations. E. G.-J. acknowledges the support of the National Science Foundation IGERT grant DGE02-21715, as well as a Cota-Robles fellowship. Computing time has been provided by the California NanoSystems Institute at the University of California at Santa Barbara and Hewlett-Packard and by the National Centre for High-Performance Computing in Taiwan.

REFERENCES

Baines, P. G. 1995 *Topographic Effects in Stratified Flows*. Cambridge University Press.

Bearman, P. W. & Zdravkovich, M. M. 1978 Flow around a circular cylinder near a plane boundary. *J. Fluid Mech.* **89**, 33–47.

Benjamin, T. B. 1968 Gravity currents and related phenomena. *J. Fluid Mech.* **31**, 209–248.

Birman, V. K., Battandier, B. A., Meiburg, E. & Linden, P. F. 2007 Lock-exchange flows in sloping channels. *J. Fluid Mech.* **577**, 53–77.

Birman, V. K., Martin, J. E. & Meiburg, E. 2005 The non-Boussinesq lock-exchange problem. Part 2. High-resolution simulations. *J. Fluid Mech.* **537**, 125–144.

Blanchette, F., Strauss, M., Meiburg, E., Kneller, B. & Glinsky, M. E. 2005 High-resolution numerical simulations of resuspending gravity currents: conditions for self-sustainment. *J. Geophys. Res.* **110**, C12022, doi:10.1029/2005JC002927.

Bonnecaze, R. T., Huppert, H. E. & Lister, J. R. 2006 Particle-driven gravity currents. *J. Fluid Mech.* **250**, 339–369.

Bonnecaze, R. T. & Lister, J. R. 1999 Particle-driven gravity currents down planar slopes. *J. Fluid Mech.* **390**, 75–91.

Bruschi, R., Bughi, S., Spinazze, M., Torselletti, E. & Vitali, L. 2006 Impact of debris flows and turbidity currents on seafloor structures. *Norw. J. Geol.* **86**, 317–337.

Cantero, M. I., Lee, J. R., Balachandar, S. & Garcia, M. H. 2007 On the front velocity of gravity currents. *J. Fluid Mech.* **586**, 1–39.

Castro, I. P. 2002 Weakly stratified laminar flow past normal flat plates. *J. Fluid Mech.* **454**, 21–46.

Chernyshenko, S. I. & Castro, I. P. 1996 High-Reynolds-number weakly stratified flow past an obstacle. *J. Fluid Mech.* **317**, 155–178.

Chomaz, J. M., Bonneton, P. & Hopfinger, E. J. 1993 The structure of the near wake of a sphere moving horizontally in a stratified fluid. *J. Fluid Mech.* **254**, 1–21.

Doligalski, T. L., Smith, C. R. & Walker, J. D. A. 1994 Vortex interactions with walls. *Annu. Rev. Fluid Mech.* **26** (1), 573–616.

Ermanyuk, E. V. & Gavrilov, N. V. 2005*a* Interaction of an internal gravity current with an obstacle on the channel bottom. *J. Appl. Mech. Tech. Phys.* **46** (4), 489–495.

Ermanyuk, E. V. & Gavrilov, N. V. 2005*b* Interaction of an internal gravity current with a submerged circular cylinder. *J. Appl. Mech. Tech. Phys.* **46** (2), 216–223.

Germano, M., Piomelli, U., Moin, P. & Cabot, W. H. 1991 A dynamic subgrid-scale eddy viscosity model. *Phys. Fluids* A **3** (7), 1760–1765.

Gonzalez-Juez, E. D., Constantinescu, S. G. & Meiburg, E. 2007 A study of the interaction of a gravity current with a square cylinder using two-dimensional numerical simulations. In *Proceedings of the 26th Intl Conf. on Offshore Mechanics and Arctic Engineering*, San Diego, California.

Greenspan, H. P. & Young, R. E. 1978 Flow over a containment dyke. *J. Fluid Mech.* **87**, 179.

Härtel, C., Meiburg, E. & Necker, F. 2000 Analysis and direct numerical simulation of the flow at a gravity-current head. Part 1. Flow topology and front speed for slip and no-slip boundaries. *J. Fluid Mech.* **418**, 189–212.

Hopfinger, E. J. 1983 Snow avalanche motion and related phenomena. *Annu. Rev. Fluid Mech.* **15**, 47–76.

Huppert, H. & Simpson, J. 1980 The slumping of gravity currents. *J. Fluid Mech.* **99**, 785–799.

Kim, H. B. & Lee, S. J. 2001 Time-resolved velocity field measurements of separated flow in front of a vertical fence. *Exp. Fluids* **31** (3), 249–257.

Koumoutsakos, P. & Leonard, A. 1995 High-resolution simulations of the flow around an impulsively started cylinder using vortex methods. *J. Fluid Mech.* **296**, 1–38.

Lane-Serff, G. F., Beal, L. M. & Hadfield, T. D. 1995 Gravity current flow over obstacles. *J. Fluid Mech.* **292**, 39–53.

Lilly, D. K. 1992 A proposed modification of the Germano subgrid-scale closure method. *Phys. Fluids* A **4** (3), 633–635.

Lowe, R. J., Rottman, J. W. & Linden, P. F. 2005 The non-Boussinesq lock-exchange problem. Part 1. Theory and experiments. *J. Fluid Mech.* **537**, 101–124.

Martinuzzi, R. & Tropea, C. 1993 The flow around surface-mounted, prismatic obstacles placed in a fully developed channel flow. *J. Fluids Engng* **115** (1), 85–92.

Mittal, R. & Balachandar, S. 1995 Effect of three-dimensionality on the lift and drag of nominally two-dimensional cylinders. *Phys. Fluids* **7** (8), 1841–1865.

Necker, F., Hartel, C., Kleiser, L. & Meiburg, E. 2002 High-resolution simulations of particle-driven gravity currents. *Intl J. Multiphase Flow* **28** (2), 279–300.

Necker, F., Härtel, C., Kleiser, L. & Meiburg, E. 2005 Mixing and dissipation in particle-driven gravity currents. *J. Fluid Mech.* **545**, 339–372.

Ooi, S. K., Constantinescu, S. G. & Weber, L. 2005 Two-dimensional large eddy simulation of lock-exchange gravity current flows. In *Proceedings of the 31st Intl Association Hydraulic Research Congress*, Seoul, Korea.

Ooi, S. K., Constantinescu, S. G. & Weber, L. 2007 Numerical simulations of lock-exchange compositional gravity currents. *J. Fluid Mech.* In press.

Pierce, C. D. 2001 Progress-variable approach for large eddy simulation of turbulent combustion. PhD thesis, Stanford University.

Pierce, C. D. & Moin, P. 2004 Progress-variable approach for large-eddy simulation of non-premixed turbulent combustion. *J. Fluid Mech.* **504**, 73–97.

Roshko, A. 1993 Perspectives on bluff-body aerodynamics. *J. Wind Engng Indus. Aerodyn.* **49** (1–3), 79–100.

Rottman, J. W. & Simpson, J. E. 1983 Gravity currents produced by instantaneous releases of a heavy fluid in a rectangular channel. *J. Fluid Mech.* **135**, 95–110.

Rottman, J. W., Simpson, J. E., Hunt, J. C. R. & Britter, R. E. 1985 Unsteady gravity current flows over obstacles: Some observations and analysis related to the phase II trials. *J. Hazard. Mater.* **11** (1–4), 325–340.

Shin, J. O., Dalziel, S. B. & Linden, P. F. 2004 Gravity currents produced by lock exchange. *J. Fluid Mech.* **521**, 1–34.

Simpson, J. E. 1997 *Gravity Currents in the Environment and the Laboratory*. Cambridge University Press.

Sohankar, A., Norberg, C. & Davidson, L. 1999 Simulation of three-dimensional flow around a square cylinder at moderate Reynolds numbers. *Phys. Fluids* **11** (2), 288–306.

Spedding, G. R., Browand, F. K. & Fincham, A. M. 1996 Turbulence, similarity scaling and vortex geometry in the wake of a towed sphere in a stably stratified fluid. *J. Fluid Mech.* **314**, 53–103.

Williamson, C. H. K. 1996 Vortex dynamics in the cylinder wake. *Annu. Rev. Fluid Mech.* **28**, 477–539.

Williamson, C. H. K. & Govardhan, R. 2004 Vortex-induced vibrations. *Annu. Rev. Fluid Mech.* **36**, 413–455.